This manuscript has recently been resubmitted to *Geochemistry, Geophysics, Geosystems* following one round of peer-review.

Insights into the nature of plume-ridge interaction and outflux of H_2O from the Galápagos Spreading Centre

Matthew L. M. Gleeson[1,2*] and Sally A. Gibson[1]

[1]Deparment of Earth Sciences, University of Cambridge, Downing Street, Cambridge, UK, CB2 3EQ.

[2]School of Earth and Environmental Sciences, Cardiff University, Park Place, Cardiff, CF10 3AT, UK

Corresponding author email: gleesonm1@cardiff.ac.uk

KEY POINTS

1. We provide volatile analyses of basalts erupted on segments of the GSC most strongly influenced by the adjacent mantle plume.
2. Channelised melt transport between the Galápagos mantle plume and GSC causes variations in crustal thickness and geochemistry.
3. Channelised flow of plume-derived volatile-rich melts contributes up to 20 – 50% of the H_2O outflux at the Galápagos Spreading Centre.

This manuscript has recently been resubmitted to *Geochemistry, Geophysics, Geosystems* following one round of peer-review.

ABSTRACT

The flow of high-temperature and compositionally-enriched material between mantle plumes and nearby spreading centres influences up to 30% of the global mid-ocean ridge system and represents a significant, but currently unconstrained, flux of volatiles out of the mantle. Here we present new analyses of H_2O, F, Cl and S in basaltic glass chips from an archetypal region of plume-ridge interaction, the Galápagos Spreading Centre (GSC). Our dataset includes samples from the eastern GSC, on ridge segments most strongly influenced by the adjacent Galápagos mantle plume, and complements published analyses of volatiles from the western GSC. We use new two-component (peridotite-pyroxenite) forward models of mantle melting to investigate the mechanism of plume-ridge interaction along approx. 1000 km of the GSC. Our results indicate that the observed geochemical and geophysical variations cannot be recreated by models which only involve solid-state transfer of material between the Galápagos mantle plume and the GSC. Instead, we show that the geochemical and geophysical data from the GSC are well-matched by models that incorporate volatile-rich melts formed at high-pressures (>3-4 GPa) in the Galápagos plume stem and transported via channelised flow to the GSC. In addition, our new models demonstrate that channelised flow of enriched, plume-derived melt can account for up to 50% of the H_2O outgassed from regions of the GSC which are most strongly influenced by the Galápagos mantle plume.

PLAIN LANGUAGE SUMMARY

Approximately one-third of the global mid-ocean ridge system is influenced by the transfer of compositionally distinct material from nearby, upwellings of anomalously-hot mantle. Transfer of this plume material to the oceanic spreading centres might represent an important mechanism of volatile loss from Earth's mantle, but there are limited constraints on the quantities of H_2O and other volatile degassing from these regions of plume-influenced oceanic spreading centres. In this study, we

evaluate the mechanism of plume-ridge interaction between the Galápagos mantle plume and the nearby Galápagos Spreading Centre (GSC) using new analyses of volatiles in basalts erupted on the ridge. The results from our new numerical models demonstrate that the geochemical and geophysical signatures of plume-ridge interaction along the GSC are best explained if the transport of deep sourced mantle material between the Galápagos mantle plume and GSC occurs as a melt rather than a solid phase. In addition, our new analyses enable us to constrain the flux of H_2O out of the GSC and demonstrate that melt channelization can account for up to 50% of the H_2O flux out of plume-influenced ridges.

1 INTRODUCTION

The majority of ocean island basalts (OIBs) are believed to form as a consequence of adiabatic decompression melting in high-temperature, and potentially lithologically-heterogeneous, mantle plumes (Asimow and Langmuir, 2003; Herzberg and Asimow, 2008; Ito and Mahoney, 2005; Métrich et al., 2014; Morgan, 1971; Sobolev et al., 2007). Higher concentrations of volatiles (such as H_2O, F, or Cl) in OIBs compared to mid-ocean ridge basalts (MORBs) reflect the volatile-rich nature of deep-sourced plume material, relative to the MORB source, and are evidence of small-fraction decompression melting at higher pressures than the anhydrous peridotite solidus (Dixon et al., 2017; Gibson and Richards, 2018; Ingle et al., 2010; Jackson et al., 2015; Koleszar et al., 2009; Métrich et al., 2014). In addition, approximately 30% of the global mid-ocean ridge (MOR) system is influenced by the lateral transfer of deep-sourced mantle plume material (Ito and Lin, 1995), and potentially represent sites of substantial volatile outgassing from the Earth's mantle (Gibson and Richards, 2018; Le Voyer et al., 2018). Nevertheless, robust estimates for the outflux of volatiles from mantle plume influenced segments of MORs are rare. In addition, there remain outstanding issues related to the role of melt channelisation in the lateral transfer of geochemically-enriched plume material between mantle plume stems and nearby spreading centres.

Over the past few decades, several hypotheses have been put forward to explain both the long and short length-scale geochemical and geophysical heterogeneities that are observed along plume-influenced regions of the global MOR system. These previously proposed hypotheses include: (i) buoyancy-driven upwelling of solid peridotite beneath ridge segments that are most strongly influenced by nearby mantle plumes (e.g. Ingle et al., 2010; Maclennan et al., 2001; Sleep, 1990); (ii) radial spreading of solid plume material, consisting of enriched blebs embedded in a depleted matrix (and the role of these enriched components on dynamic plume flow; Bianco et al., 2013; Ito and Bianco, 2014; Ito and Mahoney, 2005; Ribe, 1996; Shorttle et al., 2010); (iii) flow of solid plume material in a sub-lithospheric channel (Morgan, 1978; Schilling et al., 1982); (iv) melt transport via porous flow at the base of the lithosphere (Braun and Sohn, 2003); and (v) channelized gravitational flow of off-axis plume-derived melts in a matrix of dispersing solid plume material (Gibson et al., 2015; Gibson and Richards, 2018; Mittal and Richards, 2017; Stroncik et al., 2008; Stroncik and Devey, 2011).

Channelised, gravitational flow of volatile-rich melts in a network of channels embedded in a spreading 'puddle' of solid plume material (hypothesis (v) above) was put forward by Gibson et al. (2015) to account for the simultaneous presence of enriched basalts on the GSC and depleted basalts found in nearby regions of the northeast Galápagos Archipelago (e.g. Genovesa). Subsequently, Mittal and Richards (2017) and Gibson and Richards (2018) extended this conceptual model to account for certain enigmatic features at global sites of plume-ridge interaction (including the GSC), such as the coincidence of the intersection of non-age progressive volcanic lineaments with excess crustal thickness and short length-scale geochemical anomalies (i.e. highly-enriched basalts) on the spreading ridge.

Despite continued development in the conceptual models of plume-ridge interaction via a network of melt channels embedded in solid plume material, a detailed geochemical study focusing on the role of channelised volatile-rich melts to an individual spreading centre has yet to be undertaken. Here, we present new volatile data (H_2O, F, Cl and S) for basaltic glass chips collected from plume-influenced

segments of the GSC, including the eastern GSC where only limited volatile data previously existed (e.g. Byers et al., 1983). In combination with forward melting models of a mixed peridotite-pyroxenite mantle, our new volatile data allows us to critically evaluate whether plume-ridge interaction via channelised flow of volatile-rich melts is required to explain the long (100s of km) and short (10s of km) length-scale heterogeneities observed in basalt chemistry and crustal thickness at this single site of plume-ridge interaction. Moreover, our study is the first to evaluate the role of melt-channelisation for plume-ridge interaction in a region where enriched pyroxenitic melts are present (Gleeson et al., 2020). Finally, our new volatile data and forward models of mantle melting also allow us to estimate the outflux of H_2O from the entire region of Galápagos plume-influenced ridge.

2 GEOLOGICAL BACKGROUND

2.1 MANTLE HETEROGENEITY

Located ~1000 km off the western coast of Ecuador, the Galápagos Archipelago represents a well-known example of mantle plume related volcanism. Active and recent Holocene volcanism is observed over a wide geographic area and geochemical studies of both subaerial and submarine basaltic lavas reveal that compositional heterogeneity results from the melting of at least 4 isotopically-distinct components in the Galápagos mantle plume (Geist et al., 1998; Harpp and Weis, 2020; Harpp and White, 2001; Hoernle et al., 2000; White et al., 1993). The isotopic end-members of the Galápagos mantle plume include an isotopically depleted component and 3 isotopically enriched mantle components, that can be summarised as:

1. PLUME component - dominant in basalts from the western Galápagos archipelago (centred on Isla Fernandina), which are characterised by moderately enriched Sr, Nd and Pb isotope ratios and elevated $^3He/^4He$ ratios (~30 R/R_A; Harpp and White, 2001; Kurz et al., 2009; Kurz

and Geist, 1999). The isotopic signatures of the PLUME component resembles the 'FOZO' or 'C' global mantle end-member (Hanan and Graham, 1996; Hart et al., 1992).

2. Floreana (FLO) component – centred on the southern island of Floreana and characterised by the most radiogenic Sr and Pb isotope signatures observed anywhere in the Galápagos (Harpp et al., 2014a; Harpp and White, 2001). The FLO component is hypothesised to result from melting of ancient recycled oceanic crust (~2.2 – 2.5 Ga) incorporated in to the Galápagos plume (Gibson et al., 2016; Harpp et al., 2014).

3. Wolf-Darwin (WD) component – most prevalent in basaltic lavas from the northern islands of Pinta, Wolf, Darwin and surrounding seamounts (Harpp et al., 2014c; Harpp and White, 2001). The WD component is characterised by elevated $^{208}Pb/^{206}Pb$ and $^{207}Pb/^{206}Pb$ ratios (Harpp and White, 2001). The origin of this component remains enigmatic.

The spatial heterogeneity in the radiogenic isotope composition of basalts erupted in the Galápagos Archipelago provides insights into the structure of the underlying plume and the deep mantle. For example, isotopically enriched signatures are most commonly observed in the south-western Archipelago (corresponding to the PLUME and FLO components), whereas isotopically depleted basalts are typically found further east (Harpp and Weis, 2020; Harpp and White, 2001; Hoernle et al. 2000; White et al., 1993). This bilateral asymmetry in the composition of the upwelling mantle plume, which is similar to that observed in Hawaii and other regions of plume-derived volcanism worldwide (Harpp et al., 2014b; Weis et al., 2011), has been linked to the presence of deep mantle superstructures at the base of the Galápagos plume (Harpp and Weis, 2020). Specifically, the isotopically-enriched signatures of the south-western Galápagos have been assigned to melting of material originating in the Pacific Large Low Shear Velocity Province, whilst the isotopically-depleted signatures of the eastern Galápagos volcanoes are assigned to melting of the ambient Pacific lower mantle or entrained upper mantle material (Harpp and Weis, 2020). An outstanding complication of this picture of mantle isotopic heterogeneity in the Galápagos plume is the non-trivial relationship

between isotopic and lithological heterogeneity. Olivine minor element concentrations were originally used to indicate that both isotopically-enriched and isotopically-depleted pyroxenite components are present in the Galápagos mantle plume (Vidito et al., 2013). Nevertheless, recent models that consider the influence of magma chamber recharge on the minor element contents of magmatic olivines demonstrate that basalts sourced from the isotopically-depleted mantle component in the Galápagos are predominantly derived from a peridotitic source (Gleeson and Gibson, 2019). More recently, variations in the Fe-isotope composition of the GSC basalts have been used to show that both peridotite and pyroxenite source components contribute to the composition of plume-influenced basalts on the GSC (Gleeson et al., 2020).

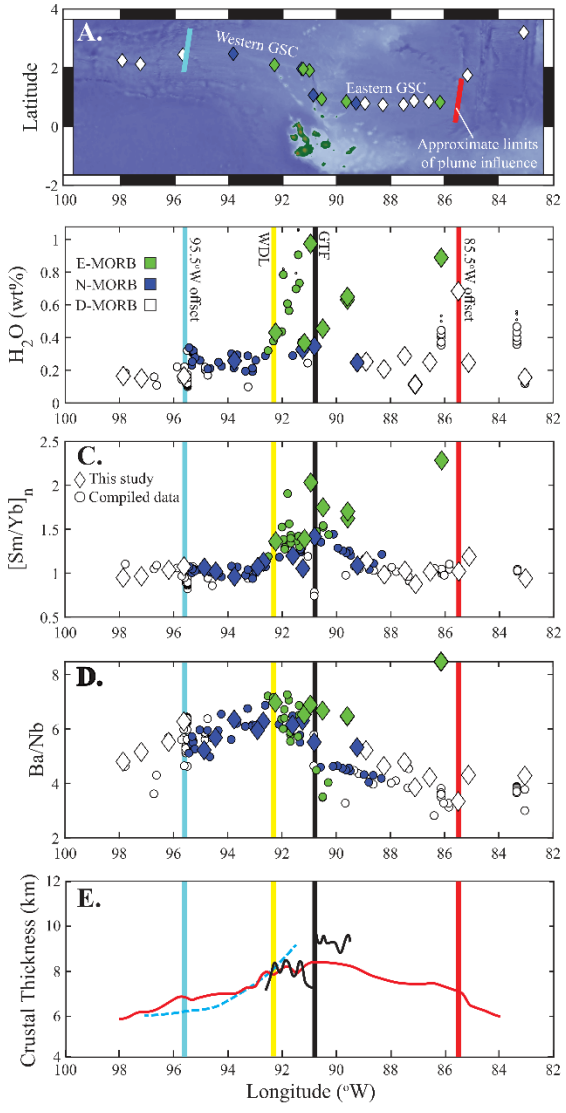

Figure 1 – *Location and chemistry of the basalts analysed from the GSC.* ***A.*** *Map of the Galápagos Spreading Centre (GSC) and Galápagos Archipelago (bathymetric data from Ryan et al., 2009).* ***B.*** *Brine-assimilation corrected H_2O contents in the GSC basalts from this study (diamonds) and from Cushman et al. (2004) and Le Voyer et al. (2018; circles). The measured H_2O contents of these basalts are shown by the small dots (only visible where large differences between the measured and corrected H_2O concentrations are seen; Supplementary Information). Panels* ***C.*** *and* ***D.*** *show key trace element ratios ($[Sm/Yb]_n$ and Ba/Nb, respectively), which display an increased contribution from melts of a garnet-bearing lithology near the Galápagos Transform Fault (GTF;* ***C.****); and a geochemical offset between the western and eastern GSC, which relates to the incorporation of the Wolf-Darwin component in the mantle beneath the western GSC (****D.;*** *data from Christie et al., 2005; Gleeson et al., 2020; Ingle et al., 2010). Crustal thickness estimates are shown in panel* ***E.*** *from Ito and Lin (1995; red), Canales et al. (2002; blue), and Mittelstaedt et al. (2014; black). 2σ error is smaller than the symbol size for all graphs. Yellow line represents the intersection of the Wolf-Darwin Lineament with the GSC. The blue and red lines represent the approximate limit of plume influence along the GSC.*

2.2 GEOPHYSICAL AND GEOCHEMICAL HETEROGENEITY ALONG THE GSC

The Galápagos Spreading Centre separates the Cocos and Nazca tectonic plates and lies ~160-250 km north of the centre of Galápagos plume upwelling, postulated from seismic tomography (Fig. 1; Hooft et al., 2003; Villagómez et al., 2014). Variations in crustal thickness and ridge morphology provide evidence for the influence of the Galápagos mantle plume along a ~1000 km wide zone of the GSC, extending between 85.5°W and 95.5°W (e.g. Christie et al., 2005; Ito and Lin, 1995). For example, a crustal thickness high is observed at ~90.5 °W, near the closest point on the GSC to the centre of the mantle plume upwelling (Canales et al., 2002; Christie et al., 2005; Detrick et al., 2002; Mittelstaedt et al., 2014).

A major transform fault at ~91°W, the Galápagos Transform fault (GTF), separates the western and eastern GSC (Fig. 1). Both ridge segments show changes in morphology, from a low-relief valley and ridge terrain to a prominent axial ridge, as the separation distance between the ridge and hotspot decreases (Christie et al., 2005; Sinton et al., 2003). Along the western GSC the depth of the seismically-imaged magma lens increases from 1-2.5 km east of 92.5°W to 2.5-4.5 km between 92.7°W and 94.7°W, corresponding to a change from fissure-fed eruptions near the GTF to point source eruptions further west (Behn et al., 2004; Blacic et al., 2004). These features are consistent with a decrease in magma supply, and as a consequence heat flux, with increasing distance from the mantle plume (Canales et al., 2014).

A prominent geochemical anomaly has been observed on the GSC near the GTF, between 89.5°W and 92.5°W (Christie et al., 2005; Ingle et al., 2010; Schilling et al., 2003). Basalts erupted within this region are characterised by elevated concentrations of strongly incompatible trace elements (e.g. Nb, La) together with radiogenic Sr and Pb and unradiogenic Nd and Hf isotope ratios (Christie et al., 2005; Gleeson et al., 2020; Ingle et al., 2010; Schilling et al., 2003, 1982). Many incompatible trace element ratios (such as Sm/Yb and Nb/Zr) display broadly symmetric profiles that are centred around ~91 – 91.5 °W, just to the west of the GTF (Fig. 1). In addition, positive correlations between trace element

enrichment and Fe-isotopes in the GSC basalts demonstrates that the plume-influenced GSC basalts are formed through melting of a lithologically heterogeneous mantle source (Gleeson et al., 2020).

Some important differences exist between the eastern and the western GSC. Firstly, the highest resolution gravity and multi-beam bathymetry data available indicates that the crustal thickness increases by ~1 km from west to east across the GTF (Mittelstaedt et al., 2014). Secondly, the eastern GSC basalts generally have lower ratios of fluid-mobile to fluid-immobile trace elements (e.g. Ba/Nb; Fig. 1) and lower $^{208}Pb/^{204}Pb$ and $^{207}Pb/^{204}Pb$ ratios than basalts from the western GSC (e.g. Christie et al., 2005; Gibson et al., 2015; Ingle et al., 2010; Schilling et al., 2003). The long length-scale east-to-west geochemical differences on the GSC have been attributed to an additional contribution of melts from the isotopically-enriched Wolf-Darwin Galápagos mantle component beneath the western GSC (Gibson et al., 2015; Ingle et al., 2010; Schilling et al., 2003).

Gibson and Richards (2018) observed a series of short length-scale geochemical and geophysical features that are superimposed on the broad length-scale heterogeneity of the GSC. For example, basalts with anomalously high H_2O contents relative to their neighbouring basalts (typically >0.4 wt.%), and short length-scale crustal thicknesses anomalies at locations where long-lived volcanic lineaments intersect the GSC (Mittelstaedt et al., 2014). As a result, it has been suggested that melt channels embedded within the 'normal' spreading of Galápagos plume material represents an important component of plume-ridge interaction (Gibson and Richards, 2018; Mittal and Richards, 2017). In this study, we use new melting models of a mixed peridotite-pyroxenite mantle to critically evaluate the role of melt channelisation from the Galápagos plume stem in generating both short and long length-scale geochemical and geophysical heterogeneity on the GSC. In addition, our new data expands the existing volatile dataset for the GSC and enables us to place improved constraints on the flux of H_2O out of the entire segment of plume-influenced ridge.

3 METHODOLOGY

Twenty-two chips of basaltic glass (1-10 mm diameter) collected at regularly spaced intervals (30-40 km) between 83 and 98°W on the Galápagos Spreading Centre were selected from the Jean-Guy Schilling collection at the University of Rhode Island, USA. Here we present new analyses of their H_2O, F, Cl, and S concentrations (Fig. 1). The major and trace element contents of the selected glasses, together with their Fe, Sr, Nd, Hf, and Pb isotope ratios, have previously been reported (Schilling et al., 2003; Gleeson et al., 2020).

Basaltic glass chips in polished epoxy mounts were analysed for sulfur on a Cameca SX100 EPMA in the Department of Earth Sciences at the University of Cambridge. Sulfur was analysed alongside the major elements (following methods described in Gleeson et al., 2020) to calculate the required matrix correction. The S concentrations were determined by counting for 90 s on the K_a peak using a beam current of 10 nA, an acceleration voltage of 15 kV, and a defocussed beam (10 µm). Data quality was checked using the VG2 basaltic glass standard (Jarosewich et al., 1980).

Prior to analysis of H_2O, F, and Cl on a Cameca ims-4f at the NERC Edinburgh Ion Microprobe Facility (EIMF), the GSC glasses were briefly re-ground and polished, to remove topography caused by prior laser ablation analysis, and gold coated. Secondary Ion Mass Spectrometry (SIMS) analysis was carried out using a $^{16}O^-$ primary ion beam and a 14.5 keV net impact energy (4.5 keV secondary ion accelerating voltage). A liquid nitrogen cold trap was used to reduce background counts on volatile elements during analysis. Both static and electrostatic magnets were applied to centre H^+ ion images relative to heavier masses. A 3 minute, 20 µm square raster pre-sputter was applied to reduce H^+ background. Analysis was then carried out using a 15-20 µm spot. Secondary ions were analysed with a 25 µm image field. Analysis of quartz crystals at regular intervals during analysis was used to determine H^+ backgrounds (< 0.02 wt%).

The SIMS data was collected over 8 cycles with total count times of 30 s for ^{1}H and 80 s for ^{19}F, 40s for ^{35}Cl, and 16s for ^{30}Si, which was used for internal standardisation. ^{1}H counts were only recorded for the final 6 cycles to avoid any contamination. H_2O concentrations for the GSC glasses were calculated using a H_2O versus $^{1}H/^{30}Si$ calibration slope calculated using analyses of BCR-2g (anhydrous) and standards St-1, St-2, and St-6 from Shishkina et al. (2010). Calibration slopes for F and Cl (F versus $^{19}F/^{30}Si$ x SiO_2 and Cl versus $^{35}Cl/^{30}Si$ x SiO_2) were determined using the composition of BCR-2g from by Marks et al. (2017). The analytical precision for H_2O (3.5%), F (8%) and Cl (16%) was determined using five repeat measurements of GSC basalt TR164 11D-1g.

4 RESULTS

Our new SIMS data represent the first systematic analyses of H_2O, F, S and Cl for well-characterised D-, N- and E-MORB erupted on the eastern GSC (geochemical divisions are the same as those used in Gleeson et al. 2020), and thus expands the published volatile dataset to cover the entire section of the Galápagos plume-influenced ridge (Cushman et al., 2004; Ingle et al., 2010; Le Voyer et al., 2018; Michael, 1995).

4.1 DEGASSING, CONTAMINATION AND FRACTIONAL CRYSTALLISATION

The volatile contents of oceanic basalts are highly susceptible to modification by degassing, contamination and crystal fractionation (Dixon, 1997; Kendrick et al., 2015; Workman et al., 2006). All of the GSC samples analysed in this study were collected at water depths >1500 m and erupted under high enough pressure to minimise loss of H_2O to a vapour phase (Dixon, 1997; Iacovino et al., 2020;

234 Shishkina et al., 2014). As a result, we estimate that degassing had only a minor influence on the H_2O

235 content of these GSC basalts (generally <2% loss; see Supplementary Information).

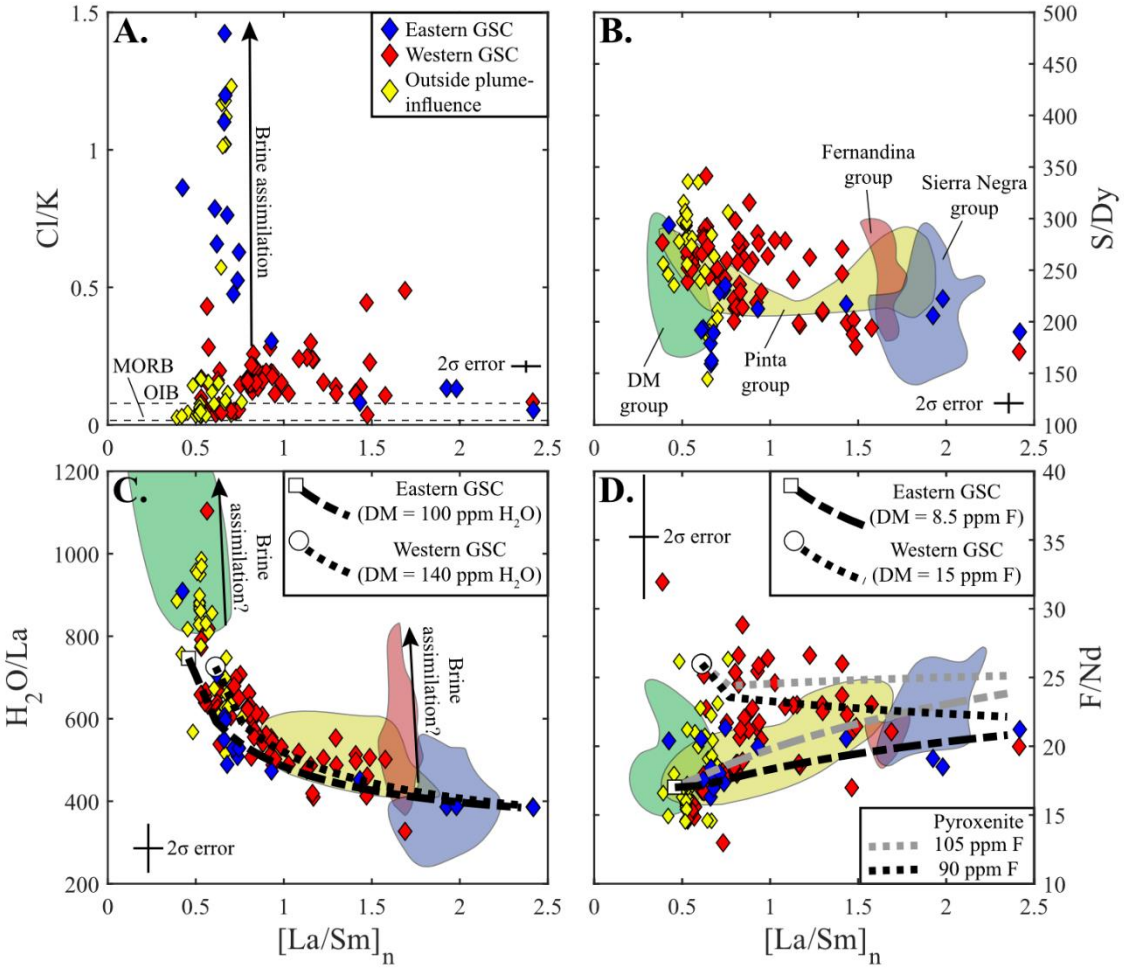

Figure 2 – *Relationship between volatile to non-volatile trace element ratios (e.g. H_2O/La) and indices of enrichment (represented here by $[La/Sm]_n$). Shown in all panels are the composition of the GSC basalts (colour coded according to location) as well as the composition of submarine basalts from the Galápagos Archipelago measured by Peterson et al. (2017) (DM group = green; Pinta group = yellow; Fernandina group = red; Sierra Negra group = blue). Panel **A.** shows that many of the GSC basalts contain higher Cl/K ratios than those typically seen in MORBs or OIBs. Panel **B.** reveals that the S/Dy ratios of GSC basalts are similar to those observed in basaltic glass chips from across the archipelago (Peterson et al., 2017). Panel **C.** shows that the H_2O/La ratio of plume-influenced GSC basalts varies from ~750 in depleted samples to <400 in the enriched samples. The white symbols and black lines show the compositions predicted by mantle melting models in this study. In all models shown, the enriched, pyroxenitic mantle component contains ~950 ppm H_2O and the black lines represent the trends predicted by increasing contribution of channelized melts from melting of this component (see Section 6). The H_2O data from the GSC has been corrected for the influence of brine assimilation whereas the data for the submarine basalts from Peterson et al. (2017) has not (as different correction factors are required for each dataset). Panel **D.** shows the variation in the F/Nd ratio of the GSC basalts. Black lines show the model predictions for increasing contribution of channelised flow where the enriched mantle end-member contains 90 ppm F. Grey lines show equivalent models for a scenario where the enriched, pyroxenitic end-member contains 105 ppm F. GSC data taken from this study (eastern GSC), Ingle et al. (2010), Cushman et al. (2004) and Le Voyer et al. (2018).*

An indication of the extent of magmatic interaction with seawater or hydrothermal brines, which can substantially influence the H_2O contents measured in submarine basalts (Kendrick et al., 2015), is provided by the Cl and K_2O concentrations of basaltic lavas. In the GSC basalts, Cl exhibits a large range (9 ppm to 3360 ppm) and almost all samples have Cl/K ratios that are much greater than those previously proposed for primary OIBs or MORBs (Fig. 2a; 0.01-0.08, with some regions up to 0.15; Kendrick et al., 2015; Le Roux et al., 2006; Michael and Cornell, 1998). We therefore suspect that GSC basalts have assimilated a Cl-rich component (that is, a brine).

We used the H_2O/Cl, K/Cl and F/Cl ratios of the GSC basalts, together with an assumed Cl/K ratio of 0.08, to evaluate and correct for the effects of brine assimilation on their H_2O contents (see Supplementary Information). Owing to the influence of brine assimilation on the Cl content of the GSC basalts, we do not attempt to constrain variations in the Cl/K or Cl/Nb ratio of their mantle source regions. Likewise, although S is commonly hypothesised to behave similarly to Dy during mantle melting (Fig. 2b; Peterson et al., 2017), recent studies have shown that concentrations of chalcophile elements (such as Se, Ag, and Cu) are required to truly evaluate the behaviour of S during mantle melting and fractional crystallisation (Reekie et al., 2019; Sun et al., 2020; Wieser et al., 2020). Since chalcophile element data is not available for our samples, we primarily focus on constraining only the H_2O and F systematics of the GSC mantle source regions.

To account for sub-ridge magma chamber processes, we have corrected the volatile data from the GSC basalts for fractional crystallisation (to 8 wt. % MgO), using the method outlined for major and trace elements by Gleeson et al. (2020) and mineral-melt volatile element partition coefficients published by Hauri et al. (2006) and Johnson (2006).

4.2 Variations in H_2O and F contents of GSC basalts

Our new SIMS data reveal that basalts from the GSC exhibit large variations in H_2O, with basalts from the western GSC reaching higher concentrations (0.10 to 1.08 wt.%; Cushman et al., 2004) than those

on the eastern GSC (0.12 to 0.87 wt.%). Fluorine contents also show large variations in the GSC basalts; as with H_2O, F concentrations display a larger range in basalts from the western GSC (70 – 838 ppm; Ingle et al., 2010) compared to the eastern GSC (92 – 579 ppm). The highest concentrations of both H_2O (>0.4 wt.%) and F (>300 ppm) typically occur in basalts erupted between 89 and 92 °W (i.e. on either side of the Galápagos Transform Fault, Fig. 1), except for a single sample (ST7 17D-1g) collected from 86.13°W on the eastern GSC (bathymetry data shows no evidence for a seamount or other topographic anomalies in this region; Ryan et al., 2009).

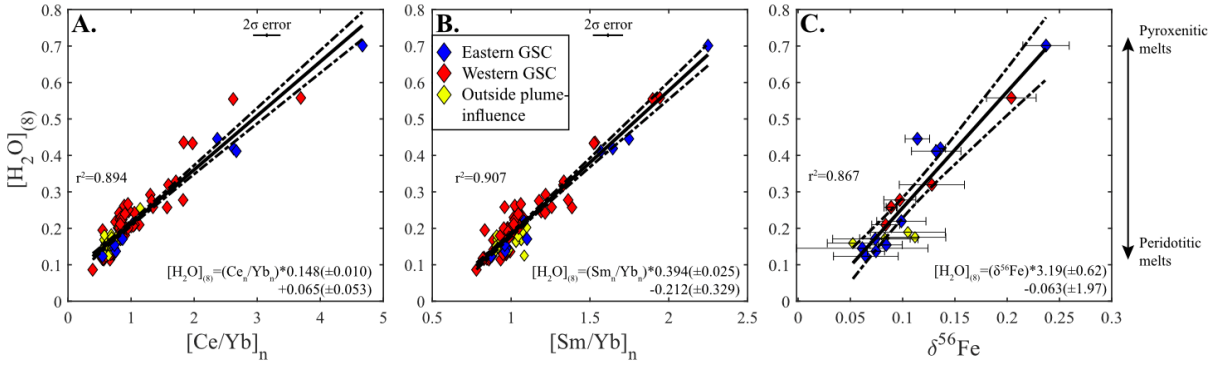

Figure 3 – *Relationship between $[H_2O]_{(8)}$ and key geochemical indices of compositional enrichment.* ***A.*** *and* ***B.*** *display the correlation between trace element proxies of geochemical enrichment/melt fraction and $[H_2O]_{(8)}$ (fractionation corrected H_2O). The correlation between $[Sm/Yb]_n$ and $[H_2O]_{(8)}$* ***(A.)*** *is used to predict the fractionation corrected H_2O concentration of the GSC basalts for which volatile data does not exist. The data displayed here has been corrected for the influence of brine assimilation (Supplementary Information).* ***C.*** *A strong correlation is observed between $\delta^{56}Fe$ and $[H_2O]_{(8)}$, which indicates that there is a contribution of volatile-rich, pyroxenitic melts to the GSC basalts. Fe-isotope data from Gleeson et al. (2020), trace element and volatile element data from this study; Cushman et al. (2004); Gleeson et al. (2020); Ingle et al. (2010); and Le Voyer et al. (2018).*

Both H_2O and F exhibit strong positive correlations with indices of trace element enrichment (such as La/Sm) in the GSC basalts (Fig. 3; Supplementary Information). Importantly, the GSC basalts with the highest H_2O and F contents (ST7 17D-1g and TR164 26D-3g) also have anomalously high $\delta^{56}Fe$ values (Gleeson et al., 2020; Fig. 3). While Sr, Nd or Pb isotope data are not available for ST7 17D-1g, we note that the volatile-rich sample TR164 26D-3g (90.95 °W) has enriched $^{87}Sr/^{86}Sr$, $^{143}Nd/^{144}Nd$ and Pb isotopic ratios relative to other GSC basalts.

5 CONSTRAINING THE VOLATILE CONTENT OF THE GSC MANTLE SOURCE

A common method for determining the volatile concentrations in the mantle source region of oceanic basalts is to measure ratios of volatile and non-volatile trace elements that exhibit similar incompatibilities during melting and crystal fractionation (Cabral et al., 2014; Jackson et al., 2015; Koleszar et al., 2009; Saal et al., 2002). Widely used ratios include H_2O/La, H_2O/Ce, F/Nd, Cl/K and S/Dy (Cabral et al., 2014; Jackson et al., 2015; Koleszar et al., 2009; Peterson et al., 2017; Saal et al., 2002) although others have been suggested (e.g. F/Zr; Le Voyer et al., 2015). In this study we use the ratios H_2O/La and F/Nd to describe the volatile systematics of the different mantle components beneath the GSC. These ratios were chosen following comparison of the behaviour of H_2O and F to non-volatile trace elements during melting of peridotitic and pyroxenitic source components (based on recent experimental constraints on the partitioning of H_2O and F in common mantle minerals; Adam et al., 2016; Dalou et al., 2012; Rosenthal et al., 2015). Notably, these mantle melting models indicate that H_2O displays similar compatibilities to La during large amounts of melting of both source components, whereas F is shown to be slightly less compatible than Nd during melting of a pyroxenitic source lithology and slightly more compatible during melting of a peridotitic source component (Fig. S.9). These models are consistent with observations from global MORBs and OIBs (e.g. Kendrick et al., 2017).

The H_2O/La ratios of the GSC basalts exhibit a negative correlation with indices of geochemical enrichment (such as $[La/Sm]_n$; Fig. 2c). Variations in the $[La/Sm]_n$ ratio of the GSC basalts could, theoretically, result from changes in the melt fraction of the mantle source; however, the anti-correlation between H_2O/La and $[La/Sm]_n$ is inconsistent with that predicted for melting of a single mantle lithology as H_2O is slightly less compatible than La during large amounts of mantle melting (Fig. S.9; Rosenthal et al., 2015). In addition, as the $[La/Sm]_n$ ratio of the GSC basalts have previously been shown to correlate with changes in the contribution of peridotite and pyroxenite-derived melts (Gleeson et al., 2020), we suggest that the H_2O/La ratio of the GSC basalts is also controlled by mixing

of melts from multiple, lithologically-distinct mantle components. Therefore, based on the maximum and minimum H_2O/La ratios measured in plume-influenced basalts from the GSC (excluding outliers), we estimate that the peridotitic and pyroxenitic components in the mantle source region of the GSC basalts have H_2O/La ratios of ~750 and ~350-400, respectively (Fig. 2).

Unlike H_2O/La, F/Nd does not display a clear relationship with indices of geochemical enrichment (e.g. $[La/Sm]_n$; Fig 2d). The eastern GSC basalts have an average F/Nd ratio of 17.6 (±7.2; including literature data), which is slightly lower than the F/Nd ratio of the western GSC basalts (20.0 ±7.3; Ingle et al., 2010). The F/Nd ratios for both the western and eastern GSC basalts lie within the range estimated for MORBs (20 ± 12; Workman et al., 2006). Notably, there is a large variation observed in the F/Nd ratios of D-MORBs from the western GSC (potentially due to the poor counting statistics of EPMA analyses at low F concentrations; Ingle et al., 2010), with many of these basalts extending to substantially higher F/Nd ratios than that observed in submarine basaltic glasses and naturally quenched melt inclusions from the Galápagos Archipelago (Fig. 2d; Koleszar et al., 2009; Peterson et al., 2017). Our new analyses for the eastern GSC basalts, however, reveal very similar F/Nd ratios to those analysed from the Galápagos Platform (Peterson et al., 2017).

To convert the H_2O/La and F/Nd ratios of the GSC basalts into mantle source volatile concentrations knowledge of the trace element compositions of the different mantle components undergoing melting beneath the GSC are required. Gleeson et al. (2020) demonstrated that the highly-depleted composition (i.e. low $[La/Sm]_n$ ratios) of the plume-influenced D-MORBs from the eastern GSC can be reproduced by melting of a peridotitic component with the trace element composition of the depleted DMM (Depleted MORB Mantle; Workman and Hart, 2005). Therefore, if we assume that the La concentration of the depleted peridotite component beneath the eastern GSC is ~0.134 ppm (Workman and Hart, 2005), and that this component is characterised by a H_2O/La ratio of ~750 (characteristic of the most-depleted plume-influenced basalts), its H_2O concentration can be

calculated to be ~100 ppm. This estimate is similar to the H_2O content estimated for depleted mantle by Michael (1988); Saal et al. (2002); Salters and Stracke (2004); and Shimizu et al. (2016,2019).

The H_2O content of the peridotitic mantle source beneath the western GSC, however, remains uncertain owing to the lack of constraints on the trace element composition of the Wolf-Darwin Galápagos mantle plume component. For the modelling shown below, we assume that the western GSC peridotite source component contains ~140 ppm H_2O, which is based on a source La content of ~0.194 ppm that is calculated through a 90:10 mixture of the depleted DMM (Workman and Hart, 2005) and the enriched mantle component of Donnelly et al. (2004). This is identical to the peridotite source used for the western GSC in the calculations of Gleeson et al. (2020), and has thus been shown to recreate the composition of N-MORBs near 95.5°W on the western GSC. As outlined above, the presence of a small amount of enriched material in this peridotitic source is consistent with the contribution of the WD mantle component to the isotopic composition of the western GSC basalts (Gibson et al., 2015).

In addition, the large uncertainty in the composition of recycled oceanic crust, and the relative contribution of recycled crust and ambient mantle peridotite to the formation of secondary pyroxenites, mean that the trace element and H_2O content of the pyroxenitic component is difficult to constrain. One possible solution was presented by Gleeson et al. (2020), who modelled the trace element composition of this component through a 50:50 mixture of recycled oceanic crust (composition from Porter and White, 2009) and the DMM, which gives a La content of ~2.73 ppm. By taking this source estimate and assuming a H_2O/La of ~350-400 for the pyroxenitic source component (see above) we estimate that the H_2O content of the pyroxenitic source in the Galápagos mantle plume is ~950 ppm. If we were to take the estimated composition of recycled oceanic crust from Stracke et al. (2003), instead of that from Porter and White (2009), then the calculated La content of the pyroxenite source would be only ~0.907 ppm, resulting in a calculated source H_2O content of 315 – 365 ppm. This demonstrates the large influence on the choice of source trace element compositions

on the estimated H_2O content of the Galápagos mantle. Nevertheless, our new data shows that the pyroxenitic component contained within the Galápagos mantle plume likely has a higher H_2O content than the isotopically depleted mantle component (>300 ppm compared to ~100 ppm).

In a similar manner to the H_2O content of the GSC mantle source, the F content of the depleted mantle component beneath the eastern GSC can be estimated from its Nd content (assumed to be ~0.483 ppm, equivalent to that of the depleted DMM; Workman and Hart, 2005) and the F/Nd of the depleted eastern GSC basalts (~16 – 18). The results of these calculations give a F content of 7.7 – 8.7 ppm, which is shown to recreate the F/Nd systematics of the eastern GSC basalts in our models of melting a 2-component mantle (Fig. 2d). Similarly, taking a source Nd concentration of ~0.558 ppm (calculated assuming a 90:10 mixture of depleted and enriched mantle for the western GSC peridotite), we can constrain the F content of the peridotitic component beneath the western GSC to 8.4 – 15.6 ppm (assuming a characteristic F/Nd ratio of 15-30), consistent with the western GSC data (Ingle et al., 2010). Finally, assuming that the F/Nd ratio of the most enriched GSC basalts (20 – 21.5) is characteristic of the pyroxenitic mantle source component, the source F concentration is calculated to be 105 – 133 ppm (source Nd concentration of 5.267 ppm taken from Gleeson et al., 2020). However, mantle melting models that incorporate recent experimental constraints on F partitioning during mantle melting (Adam et al., 2016; Dalou et al., 2012) reveal that a pyroxenitic source F concentration of ~105 ppm overestimates the F/Nd ratio of the most enriched GSC basalts (owing to the slightly more incompatible nature of F than Nd during melting of a pyroxenitic lithology; Fig. 2d; Fig. S.9; Fig. S.10). Therefore, to provide more robust constraints on the F content of the pyroxenitic mantle source, we iteratively adjusted the concentration of F in our mantle melting models until the model predictions (generated by varying the proportion of plume-derived channelised melt to the GSC; see Section 6) matched the GSC data. The results indicate that our new data is best matched when the pyroxenitic F content is set at ~90 ppm.

This manuscript has recently been resubmitted to *Geochemistry, Geophysics, Geosystems* following one round of peer-review.

6 NUMERICAL MODELS OF GALÁPAGOS PLUME-RIDGE INTERACTION

6.1 SIMULATING MANTLE MELTING

Early models of plume-ridge interaction related compositional variations in plume-influenced MORBs to chemical heterogeneity on the scale of 10s to 100s of km in the sub-ridge mantle (i.e. erupted magma compositions are directly related to the bulk composition of the underlying mantle; Schilling, 1991; Schilling et al., 2003, 1982; Verma and Schilling, 1982). Such models suggested that isotopically and incompatible trace element enriched plume material flows towards, and then along, the ridge axis where it becomes progressively diluted by mixing with ambient asthenosphere.

These early models recreated some of the geochemical features that are observed along plume-influenced ridges; however, they are difficult to reconcile with dynamical models that predict no significant solid-state mixing between plume and ambient mantle (Farnetani and Richards, 1995; Ito et al., 2003, 1997). For this reason, more recent studies of plume-ridge interaction have focused on a second class of model, where mantle heterogeneity is important on length-scales of ~1 km or less (Ingle et al., 2010; Ito and Mahoney, 2005). In this type of model, the solid sub-ridge mantle is composed of a near constant mixture of enriched, hydrous peridotite or pyroxenite 'blebs' in a depleted (anhydrous) peridotite matrix. Owing to their different volatile contents and/or lithological properties, the enriched blebs undergo melting at greater depths than the surrounding anhydrous peridotite (Ingle et al., 2010; Ito et al., 1997). Previous studies that have applied these models to the GSC have concluded that variations in basalt chemistry and crustal thickness are due to intermediate scale variations in mantle flow and/or melt extraction from the underlying mantle (Ingle et al., 2010; Ito and Bianco, 2014; Ito and Mahoney, 2005; Shorttle et al., 2010).

To place improved constraints on the mechanisms of Galápagos plume-ridge interaction, we use new two-component mantle melting models that build on the second class of models described above.

Specifically, our models simulate melting of a mixed lithology mantle (peridotite and pyroxenite; based on the Melt-PX parameterization of Lambart et al., 2016) and we innovate by including calculations that account for the contribution of channelized, volatile-rich melts formed by melting of a pyroxene-rich mantle component in the Galápagos plume stem (Gleeson et al., 2020). By simulating the melting of a mixed lithology mantle our models differ from those of previous studies that have considered only peridotite source components (Gibson and Richards, 2018; Ingle et al., 2010). While we acknowledge that the role of pyroxenite is controversial, and more work needs to be done, the key findings of our models for the mechanisms of plume-ridge interaction, are to a large extent, independent of the source lithology chosen for the enriched mantle component in the source region of the GSC basalts (i.e. peridotite vs pyroxenite).

By incorporating the trace element engine outlined in Gleeson et al. (2020), our new models allow us to test the influence of the rate of mantle upwelling; depth at which melting ceases; and the contribution of channelised, plume-derived melts on the crustal thickness of the ridge and the trace element chemistry of the GSC basalts (see Supplementary Information). The initial non-volatile trace element composition of the various mantle components beneath the GSC are identical to those used in Gleeson et al. (2020). In all of our models, the trace element partition coefficients were calculated using the model of Gibson and Geist (2010) and mineral-melt partition coefficients for H_2O and F were taken from recent experimental data (Adam et al., 2016; Dalou et al., 2012; Rosenthal et al., 2015).

We recognise that the parameterisations of Lambert et al. (2016) in Melt-PX are based on experiments conducted between 1 and 4.5 GPa which do not consider the effects of volatiles on the pyroxenite solidus. Analyses of natural samples of mantle pyroxenites have, however, shown that they have a greater capacity to host volatiles than peridotites (Gibson et al., 2020). Since elevated volatile concentrations may significantly affect the location of the pyroxenite solidus, and also the melt productivity with depth, more experimental work is required to accurately parameterise the effects of H_2O on pyroxenite melting, as has been done for peridotites (Katz et al., 2003). In our forward

models of fractional melting we have used the upper H_2O estimate of 950 ppm for the pyroxenite source because this reproduces the volatile vs trace element systematics of the GSC basalts (see Section 5). We accept, however, that because of uncertainties in the depth of melting of volatile-bearing pyroxenite this is a non-unique solution.

Using our new models of mantle melting, we calculate the hypothetical composition of magmas produced at ~0.02° intervals along the GSC when variations in key mantle parameters (such as T_P; the maximum mantle upwelling velocity; and the contribution of channelised plume-derived melts) are invoked to determine the dominant mechanism of plume-ridge interaction in the Galapagos. First, we examine the extent to which the long and short length-scale geochemical and geophysical features of plume-ridge interaction on the GSC can be recreated if we assume only solid-state flow between the Galápagos mantle plume and GSC, as proposed by Ingle et al (2010), Shorttle et al. (2010) and Ito and Bianco (2014). We then highlight areas where solid-state plume-ridge interaction models poorly match the available data, and examine whether additional transport of volatile-rich melts in long-lived melt channels (Gibson and Richards, 2018) can account for these discrepancies.

6.2 ALONG-RIDGE VARIATIONS IN GSC BASALT GEOCHEMISTRY AND CRUSTAL THICKNESS PREDICTED BY SOLID-STATE FLOW

In the models of solid-state plume-ridge interaction shown below, it is assumed that variations in basalt chemistry and crustal thickness along the GSC are primarily related to changes in the rate of mantle upwelling below the anhydrous peridotite solidus (Cushman et al., 2004; Gibson and Richards, 2018; Ingle et al., 2010; Ito and Bianco, 2014; Maclennan et al., 2001; Shorttle et al., 2010). Variations in mantle upwelling velocity are hypothesized to occur as a result of the excess buoyancy flux of mantle plumes and the rapid increase in mantle viscosity associated with olivine dehydration following the onset of mantle melting (Hirth and Kohlstedt, 2003, 1996). In all models, the proportion of peridotite and pyroxenite in the mantle source is kept constant within an individual ridge segment,

443 consistent with the limited mixing between plume material and the surrounding ambient mantle
444 predicted by Ito et al. (1997). The relative rate of mantle upwelling at the base of the melt column ($U_{r\text{-}max}$; velocity defined relative to the velocity of passively upwelling mantle) is assumed to follow an
446 exponential decay curve with longitude (Table 1), with maximum values close to the GTF, after the
447 modelling of Ingle et al. (2010) and qualitatively follows the change in upwelling velocities predicted
448 by the 3D numerical model of Ito and Bianco (2014).

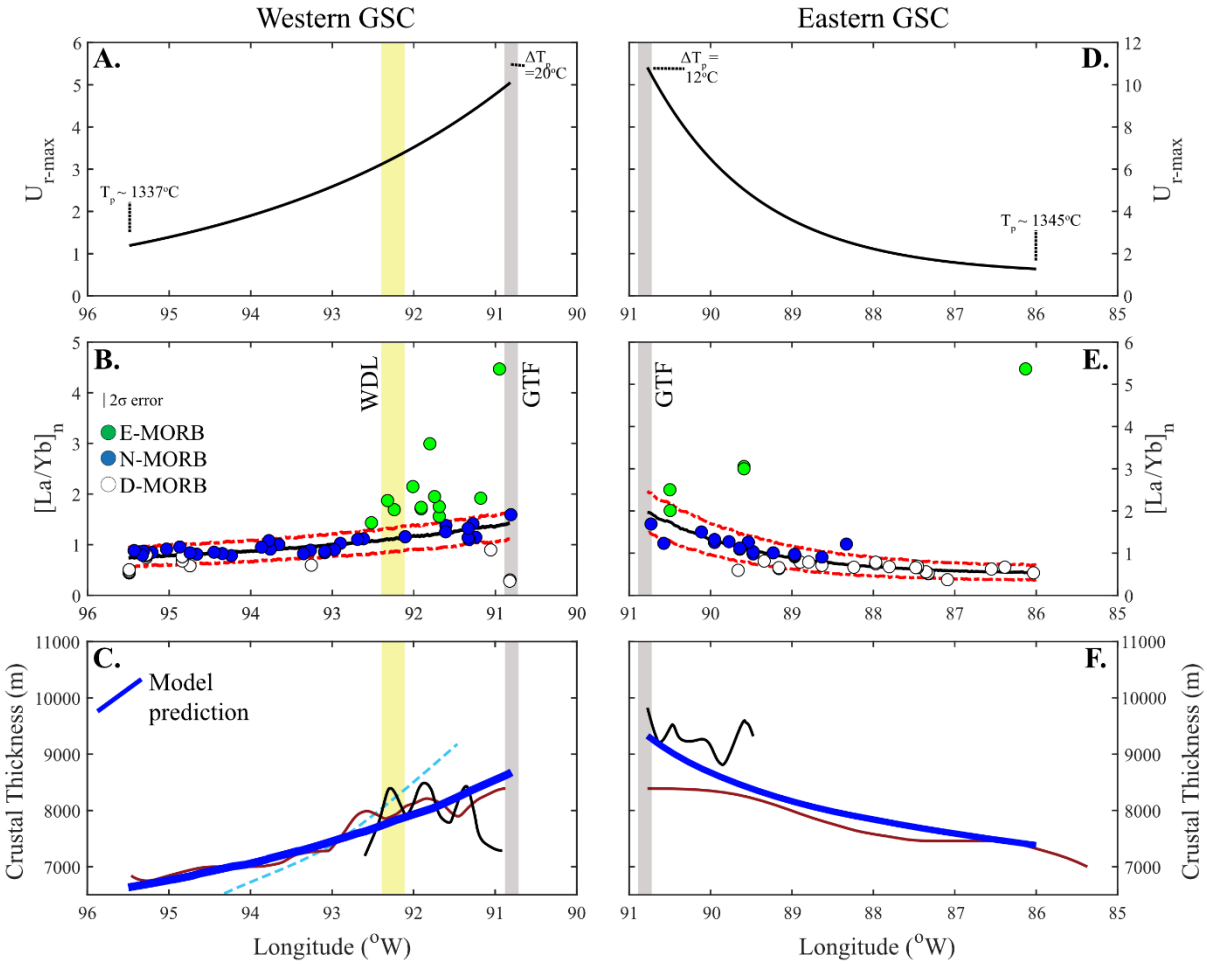

Figure 4 – *Results of plume-ridge interaction models that only account for solid-state transport between the Galápagos mantle plume and the GSC. Panels **A. - C.** show the results for the western GSC and panels **D. - F.** show the results for the eastern GSC. Panels **A.** and **D.** show the input parameters for these models, and the geochemical (**B.** and **E.**) and crustal thickness (**C.** and **F.**) results are shown below. Black lines in **B.** and **E.** display the mean composition of melts delivered to that section of ridge. The red dashed lines show the range of compositions predicted using a Dirichlet mixing function (N=500). Crustal thickness estimates are from Ito and Lin (1995; red), Canales et al. (2002; blue), and Mittelstaedt et al. (2014; black); modelled crustal thickness is shown in blue (solid line). Some of the long length-scale trends in geochemical enrichment are reproduced along the GSC; however, several discrepancies can be observed between the model predictions and the crustal thickness and geochemical data from the GSC.*

449 The mantle potential temperature (T_p) and the rate at which this changes along the ridge axis, the
450 maximum value of $U_{r\text{-}max}$, and the rate at which this decays away from the GTF, were iteratively
451 adjusted until our models produced a satisfactory match to both the composition of the GSC basalts
452 and the crustal thickness estimates of Canales et al. (2002) and Mittelstaedt et al. (2014). Figure 4
453 shows the melt compositions and crustal thicknesses produced using this method, along with the
454 range of compositions that would be expected if melts produced by decompression melting in the
455 sub-ridge region are not completely homogenised prior to eruption (calculated using a Dirichlet
456 function; N=500, where N represents the extent of mixing; Rudge et al., 2013).

457 Our model results indicate that solid-state plume-ridge interaction produces an excellent match to the
458 composition of most basalts erupted west of 86°W on the eastern GSC, and the D-MORBs and N-
459 MORBs located on the western GSC (Fig. 4). In addition, the model results reveal clear differences
460 between the eastern and western GSC. For example, to generate the greater crustal thickness of the
461 oceanic crust produced along the eastern GSC (Mittelstaedt et al., 2014) our models indicate that the
462 T_P beneath the eastern GSC is slightly higher (~5-15°C) than that beneath the western GSC. This east-
463 to-west difference in mantle T_P is readily explained by the relative proximity of the eastern GSC to the
464 Galápagos mantle plume.

465 Figure 4 also highlights several pitfalls that are associated with solid-state plume-ridge interaction
466 models that account for lateral variations in mantle upwelling velocity. For example, modelled crustal
467 thickness increases systematically along the western GSC towards the GTF, which is qualitatively
468 consistent with the crustal thickness variations predicted in numerical simulations of mantle flow for
469 on-axis (or near-axis) mantle plumes (e.g. Iceland; Bianco et al., 2013). Recent studies have, however,
470 shown that there are ~20 km wide regions between ~91.8°W and the GTF with crustal thickness
471 anomalies of ~1 km (Mittelstaedt et al., 2014), which our simple model of solid-state plume-ridge
472 interaction cannot capture (Fig. 4). In addition, although the solid-state plume-ridge interaction model
473 shown in Fig. 4 accurately recreates the chemistry of the western GSC N-MORBs located west of 92.5

474 °W and east of 91.8 °W, they are not able to recreate the composition of the more enriched basalts
475 located between 92.5°W to 91.8°W, or the compositions of anomalously enriched basalts that are
476 present between 89.5 and 92°W on the GSC.

477 Some of these discrepancies may be addressed if we consider non-symmetric spreading of solid plume
478 material. To avoid depletion of the source components in volatiles and incompatible trace elements,
479 this solid state transport would need to occur below the pyroxenite solidus (i.e. >3-4 GPa). However,
480 dynamical models indicate that lateral transport of plume material typically occurs at substantially
481 lower pressures, near the anhydrous peridotite solidus or the lithosphere-asthenosphere boundary,
482 where clear changes in the rheological properties of the mantle are present (Ito and Bianco, 2014). In
483 addition, some of the offsets between our model predictions and the GSC data may result from the
484 use of a 2D model scenario to describe a 3D system. In particular, the influence of transform faults on
485 upper mantle dynamics is not considered here, but could influence the composition of basalts erupted
486 close to these structures (Weatherley and Katz, 2010). Nevertheless, we believe that this is unlikely to
487 account for the shortcomings of the solid-state plume ridge interaction models.

488 6.3 CHANNELISED FLOW OF H_2O-RICH MELTS TO THE GSC

489 Numerical models of mantle melting beneath oceanic spreading centres have shown that highly
490 permeable melt channels are a natural consequence of melting during upwelling of a heterogeneous
491 mantle (Katz and Weatherley, 2012; Weatherley and Katz, 2012). As channelised melt flow is expected
492 to restrict chemical interaction of channelised melts with the surrounding mantle (Weatherley and
493 Katz, 2012) it might represent an efficient method of transporting geochemically enriched material to
494 nearby spreading centres. In addition, highly-permeable melt channels have been shown to be
495 thermodynamically stable over distances up to ~1000 km and the transport timescales of volatile-rich
496 melts in these channels are significantly lower than the timescales required by U-series disequilibria
497 (Kokfelt et al., 2005; Mittal and Richards, 2017). Therefore, conceptual models involving the delivery

of plume-derived compositionally-enriched melts to MORs in highly permeable melt channels have been proposed for the Galápagos and other sites of plume-ridge interaction worldwide (Gibson et al., 2015; Gibson and Richards, 2018; Mittal and Richards, 2017). In these models, the primary factor driving the migration of melts from the stem of the upwelling plume (>60 – 80 km depth) to the sub-ridge mantle (<40-60 km depth) is melt buoyancy. Melt channelisation was likely initiated when the Galápagos plume was on-axis (at >5 Ma; Gibson et al. 2015) and has been maintained during ridge migration away from the plume stem.

6.3.1 Variations in the supply of channelized melts to the western and eastern GSC

The solid-state plume-ridge interaction models described in Section 6.2 require relative mantle upwelling velocities ($U_{r\text{-}max}$) of ~10 to explain the geochemical and geophysical signatures of plume-ridge interaction between 90.5°W and 90.8°W (Fig. 4). Values of $U_{r\text{-}max}$ up to ~15 have previously been suggested, based on the buoyancy flux of the Galápagos mantle plume (Ingle et al., 2010; Sleep, 1990), but more recent numerical simulations of Galápagos plume-ridge interaction indicate that the maximum relative upwelling velocity is only ~3 (~75 mm/yr compared to a velocity of ~25 mm/yr for passive mantle upwelling; Ito and Bianco, 2014). Additionally, U-series disequilibria from Saal et al. (2000) indicate that mantle upwelling velocities beneath western parts of the Galápagos Archipelago are only ~70 mm/yr, similar to the maximum upwelling velocities predicted by Ito and Bianco (2014), slightly higher than those calculated by Gibson and Richards (2018; 40 mm/yr) and much less than those required by the models of solid-state plume-ridge interaction presented above (>250 mm/yr, assuming a passive upwelling velocity of ~25 mm/yr; Ito and Bianco, 2014; Fig. 4).

As a result, in the following models we assume that: (i) the change in the relative mantle upwelling velocity across the anhydrous peridotite solidus is minimal ($U_{r\text{-}max}$ <3); and (ii) variations in the geochemical and geophysical signatures of plume-ridge interaction along the GSC are primarily derived from slight changes in T_P and/or the supply of channelised melts from the Galápagos plume stem (Table 1). The volatile and non-volatile trace element composition of the channelised melts are

calculated as the non-modal aggregated fractional melt following ~10% decompression melting of a pyroxenitic mantle component below the anhydrous peridotite solidus (>3 GPa); this represents the approximate melt fraction of the pyroxenite source component at the pressure and temperature of the anhydrous peridotite solidus (silica-deficient pyroxenite M5-40; Lambart et al., 2016).

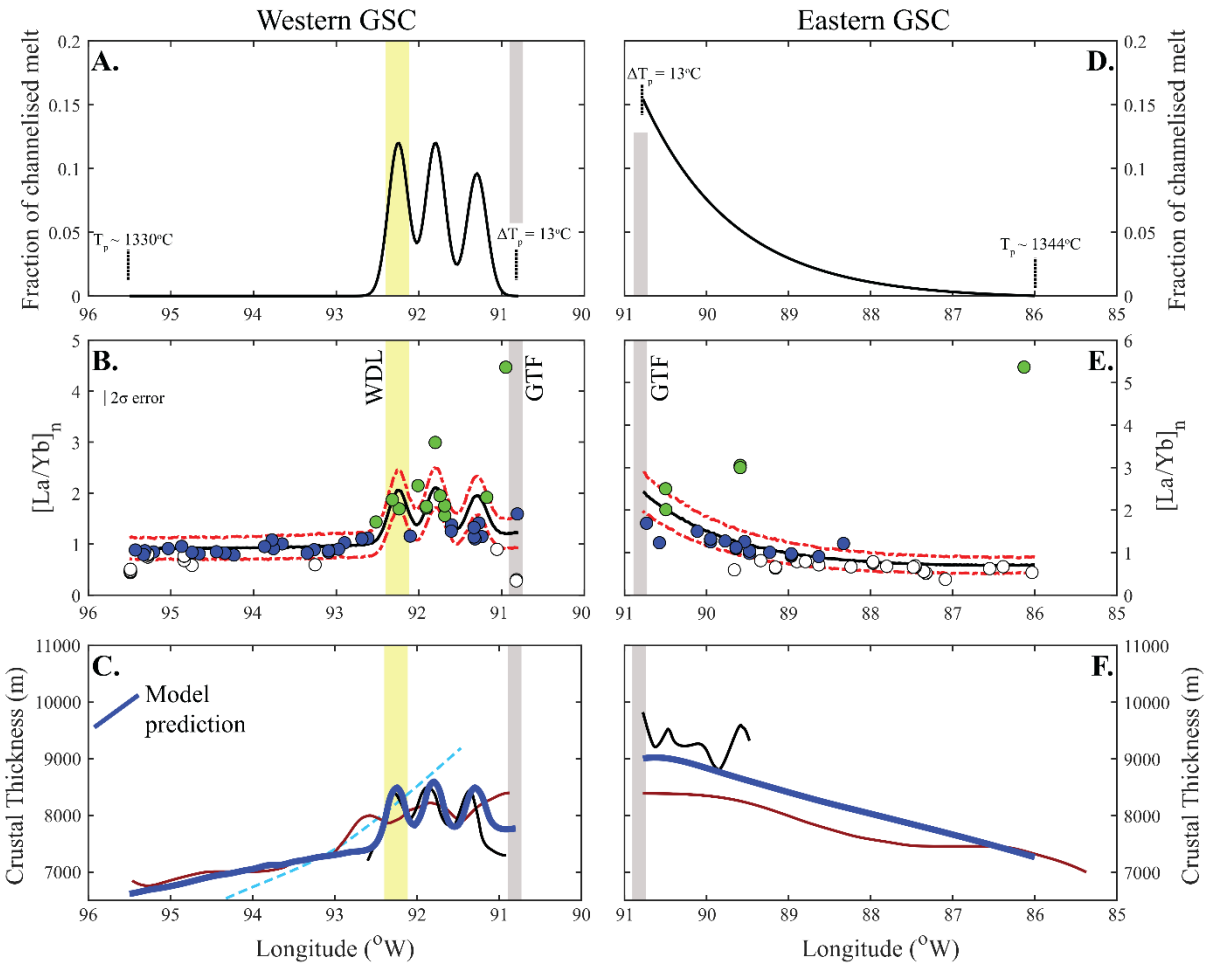

***Figure 5** - Results of plume-ridge interaction models that account for channelised melt transport between the Galápagos mantle plume and the GSC. Panels **A.** - **C.** show the results for the western GSC and panels **D.** - **F.** show the results for the eastern GSC. Panels **A.** and **D.** show the input parameters for these models (i.e. the fraction of channelised melt), and the geochemical (**B.** and **E.**) and crustal thickness (**C.** and **F.**) results are shown below. The red dashed lines show the range of compositions predicted using a Dirichlet mixing function (N=500). Crustal thickness estimates are from Ito and Lin (1995; red), Canales et al. (2002; blue), and Mittelstaedt et al. (2014; black); modelled crustal thickness is shown in blue (solid line). It can be observed that, by assuming channelised flow occurs beneath the volcanic lineaments of the Northern Galápagos Volcanic Province, the crustal thickness and geochemical signature of the basalts from the western GSC are more accurately reproduced in this model than in the model of solid-state plume-ridge interaction shown in Fig. 4.*

The crustal thickness and geochemical characteristics of the eastern GSC were generally well matched by our solid-state models of plume-ridge interaction. Nevertheless, we recognise that this is not a unique solution as these observations can also be reproduced if we model an exponential decrease in

the proportion of channelized melts supplied to the eastern GSC with increasing distance to the centre of plume upwelling (Fig. 5). In this model, the decrease in the supply of channelized, enriched melt to the eastern GSC with increasing distance to the Galapagos plume can be primarily assigned to the increased angle at which melt channels are likely to intersect the ridge axis, resulting in a reduction in the influence of channelised melt transport to the ridge at any location. This hypothesis shares many similarities to the model proposed for solid-state plume-ridge interaction by Shorttle et al. (2010), but has the advantage of being able to simultaneously explain the enriched geochemical signatures along the GSC and the depleted isotopic compositions of the island of Marchena and Genovesa in the Northern Galápagos Volcanic Province (Gibson et al., 2015; Harpp et al., 2014c).

At the closest point to the Galápagos Archipelago, the eastern GSC is located only ~100-150 km north of the centre of plume upwelling. In their theoretical study, Mittal and Richards (2017) showed that over such short plume-ridge separation distances, melt channels <4 m in radius as likely to be thermodynamically stable (assuming a constant heat flux source). We suggest, therefore, that the delivery of compositionally-enriched melts to the eastern GSC in a dense network of small melt channels embedded within a spreading puddle of plume material, as envisaged by Gibson et al. (2015), might lead to effective homogenization of mantle melts over the length-scale at which variability in geochemical compositions are typically measured. A steadily declining supply of enriched melts is then observed on the eastern GSC with increasing distance to the Galápagos mantle plume, owing to the intersection angle of the melt channels and the ridge as well as the declining proportion of melt channels that will remain thermodynamically stable over the increased melt transport distances. The continued presence of channelised melts along the whole of the eastern GSC, even if only in very small proportions (<1%), maintains the possibility that anomalously enriched basalts can be observed at the surface at plume-ridge interaction distances in excess of 300 – 400 km (see Section 6.3.2). However, the coincidence of a ~10 km wide crustal thickness anomaly (Mittelstaedt et al., 2014) and two anomalously volatile-rich samples (TR164 6D-1g and 2g, which lie outside the compositions predicted

555 by our along-ridge models; Fig. 5) at 89.5°W indicate that there may be some localised variations in
556 the volume of melt delivered to the eastern GSC that are not captured in our model.

557 The geochemical and geophysical features observed on the eastern GSC can, therefore, be produced
558 theoretically by both solid-state and two-phase models of plume ridge interaction. Many of the
559 discrepancies between the GSC data and solid-state models of plume-ridge interaction occur,
560 however, on the western GSC (e.g. the composition of basalts located between the 92.5°W and 91.8
561 °W)

562 Our modelling reveals that the geochemical and geophysical signatures of plume-ridge interaction on
563 the western GSC cannot be produced by a similar model to that used to recreate the eastern GSC data
564 (i.e. a gradually decreasing supply of channelised melts with increasing plume-ridge distance). Instead,
565 we find that the discrepancies between the western GSC geochemical and geophysical data and our
566 solid-state plume-ridge interaction models can be overcome by modelling focused delivery of
567 channelized melts to the western GSC beneath each of the three volcanic lineaments in the northern
568 Galápagos (Fig. 5), as proposed by Mittal and Richards (2017) and Gibson and Richards (2018). In the
569 model used here, the proportion of channelized melt supplied to the western GSC is assumed to follow
570 3 overlapping normal distributions, where the greatest rate of supply occurs at the intersection of
571 each of the three volcanic lineaments with the GSC (92.25°W, 91.8°W, 91.3°W). The results provide
572 an excellent match to the geochemical data (including volatiles) from the western GSC and reproduce
573 the short length-scale variations in crustal thickness observed at the intersection of each of the
574 volcanic lineaments with the western GSC (Mittelstaedt et al., 2014). It is important to note, however,
575 that the compositional variability between the different seamounts and islands that make up the three
576 volcanic lineaments indicates that their magmatic systems are primarily fed by magmas during
577 adiabatic decompression melting beneath the lineament and/or GSC (Harpp et al., 2014c).

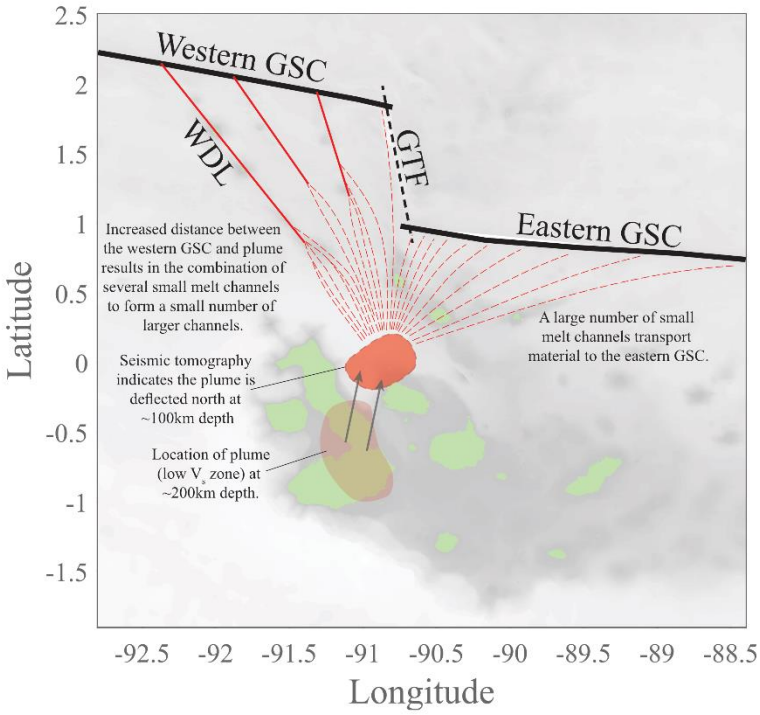

Figure 6 – *Schematic diagram illustrating the nature of the melt channels beneath the northern Galápagos volcanic province. The eastern GSC is fed by a large number of small melt channels and the influence of these melt channels declines with increasing distance to the mantle plume. On the western GSC our models predict that the melt channels amalgamate into three larger channels that are located beneath each of the three volcanic lineaments in the northern Galápagos volcanic province. The location of the Galápagos mantle plume at depths of 200 and 100 km is taken from Villagómez et al. (2014).*

578 Notably, the models used to recreate the geochemical and geophysical signatures of plume-ridge
579 interaction along the western and eastern sections of the GSC are very different. We suggest that
580 these may arise from the greater plume-ridge distance of the western GSC compared to the eastern
581 GSC (~100 km greater). This is in agreement with the hypothesis that melt channels might amalgamate
582 into a small number of larger channels over increased plume-ridge distance, resulting in the localised
583 delivery of compositionally enriched melts to 3 locations on the western GSC (Mittal and Richards,
584 2017; Gibson and Richards, 2018; Fig 6). This coalescence also helps maintain the thermodynamic
585 stability of the melt channels over the greater plume-ridge distance (Fig. 6; Mittal and Richards, 2017).

6.3.2 Anomalously enriched GSC basalts

The above models of plume-ridge interaction via channelised transport of volatile-rich melts accurately recreate the broad-scale, and some of the short length-scale, geochemical and geophysical features of plume influence on the GSC. There are, however, a series of basalts located along plume-influenced segments of the GSC (and in other regions of plume-ridge interaction worldwide) that display compositions which are too enriched to be explained by any of the models outlined above (e.g. TR164 6d-1g at 89.59 ^{o}W; Gibson and Richards, 2018). These anomalously enriched basalts, which typically contain $[H_2O]_{(8)}$ contents >0.4 wt%, have previously been explained through the localised delivery of large volumes of channelised melt to the ridge, overwhelming the contribution of more depleted melts formed in the shallow mantle (Gibson and Richards, 2018; Mittal and Richards, 2017). To build on this previous work, we use a Markov Chain Monte Carlo approach to determine the proportion of enriched melt that contributes to each of the anomalously enriched basalts located along the GSC.

In detail, the proportion of channelized melt that is required to explain the geochemical composition of the anomalously volatile-rich samples from the GSC is determined using mantle melting models that combine the composition of melts produced by adiabatic decompression melting beneath the ridge axis with channelised, enriched melts that formed in the Galápagos plume stem. For each sample 5000 models were run and in each model iteration the mantle potential temperature, the depth that melting ceases, the proportion of pyroxenite in the mantle source and the mass fraction contribution of channelized melt were randomly generated within pre-set bands (i.e. the prior distribution). A likelihood function was then used to determine the fit between the melt composition predicted in each model and the observed trace element composition of the sample under consideration (as in Gleeson et al., 2020). The results are then used to generate posterior distributions for the proportion of channelised melt that is required to explain the trace element composition of each of the anomalously enriched basalts from the GSC (Fig. 7).

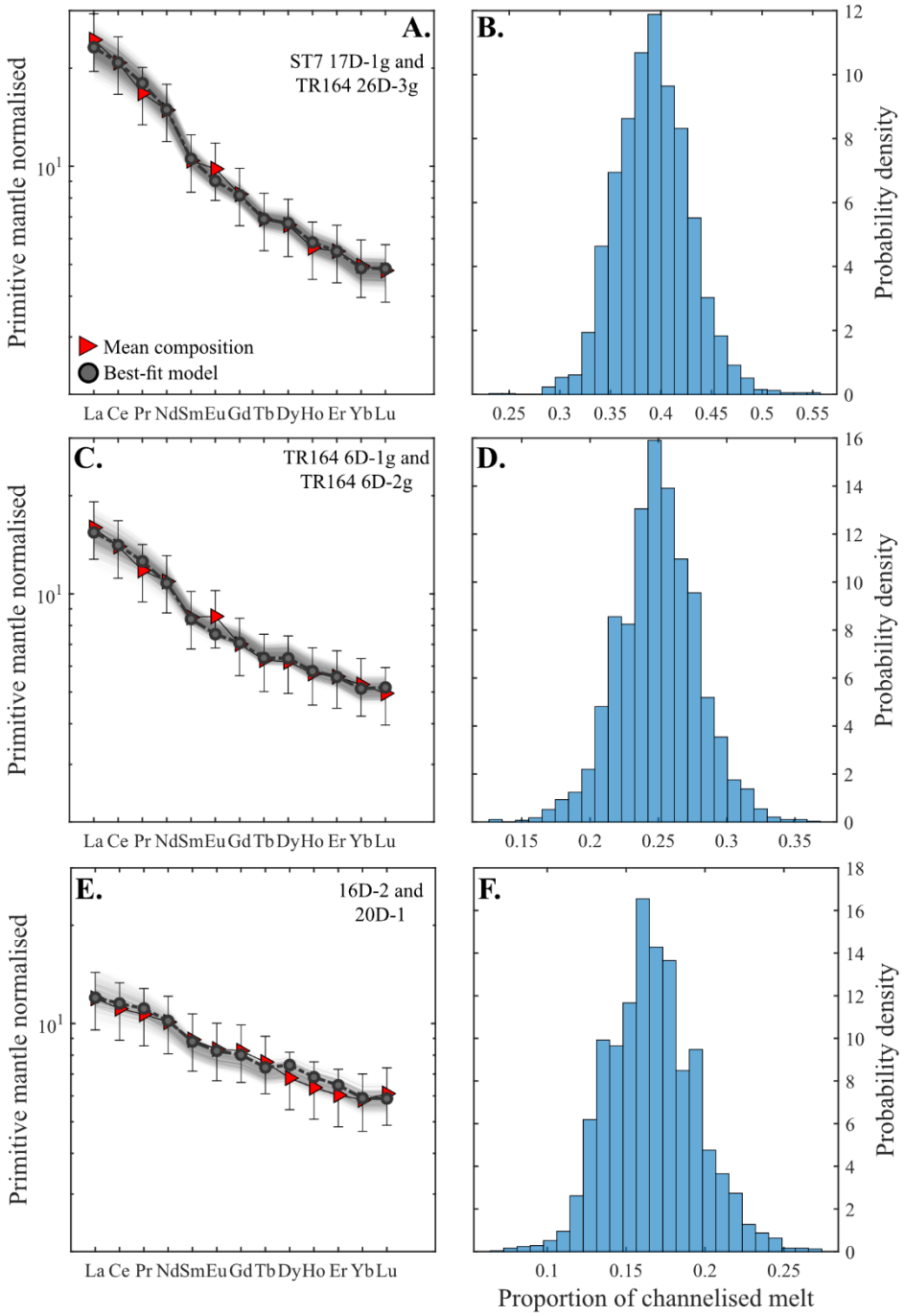

Figure 7 – *The results of our Markov Chain Monte Carlo algorithms, designed to constrain the proportion of channelised melt that contributes to each of the anomalously enriched GSC basalts. The observed trace element compositions and results of the best-fit models are shown for:* ***A.*** *the two most enriched basalts found on the GSC, ST7 17D-1g (86.13°W) and TR164 26D-3g (90.95°W);* ***C.*** *anomalously enriched basalts TR164 6D-1 and TR164 6D-2g from the eastern GSC (89.59°W); and* ***E.*** *moderately enriched basalts 16D-2 and 20D-1 (91.75 and 92.01°W; Ingle et al., 2010) from the western GSC. Panels* ***B.****,* ***D.****, and* ***F.*** *display posterior distributions for the proportion of channelised melt that contributes to each of these GSC basalts.*

611 The model predictions demonstrate that the two most enriched basalts from the GSC, which have

612 $[H_2O]_{(8)}$ contents >>0.5 wt%, likely contain a ~40% contribution of channelised, plume-derived melts

(Fig. 7). Similarly, the composition of the two samples located on the short length-scale crustal thickness high at 89.59 °W on the eastern GSC are matched by models that include a ~25% contribution of plume-derived channelised melts (Fig. 7). However, the large proportion of channelised melt required to recreate the composition of these anomalously enriched basalts is inconsistent with the magnitude of the crustal thickness anomalies found in these locations (Mittelstaedt et al., 2014). For example, at ~89.59 °W on the eastern GSC, where a crustal thickness anomaly of ~1 km is observed (~9.5 km thick crust compared to the model predictions of ~8.5 km), the 25% contribution of channelised melt required to reproduce the geochemical signature of the highly enriched GSC basalts would, in theory, generate a crustal thickness anomaly >2km. The discrepancy between the predicted and observed crustal thickness is even greater at the location of sample TR164 26D-3g (90.95 °W) where no crustal thickness anomaly is observed, but a ~40% contribution of channelised melt is required to reproduce the trace and volatile element systematics of the erupted basalt.

We therefore suggest that the extremely high proportion of channelized melt required to generate the composition of the most volatile-rich GSC basalts results from inefficient mixing of these channelised melts with those produced at shallower depths in the sub-ridge mantle (Fig. 8). In this scenario, volatile-rich basaltic magmas may reach the surface even in regions where there is a relatively low flux of channelized plume-derived melts to the GSC (Fig. 8). In fact, the low melt flux at large plume-ridge interaction distances (e.g. sample ST7 17D-1g; 86.13 °W), and locations that are proximal to large transform faults (e.g. samples TR164 26D-3g; 90.95 °W, respectively), might restrict the formation of a steady-state magma chambers (Le Voyer et al., 2015; Sinton and Detrick, 1992). As a result, it is possible that magma homogenisation is subdued at these locations, increasing the probability of enriched basalts being observed at the surface (Langmuir and Bender, 1984; Le Voyer et al., 2015).

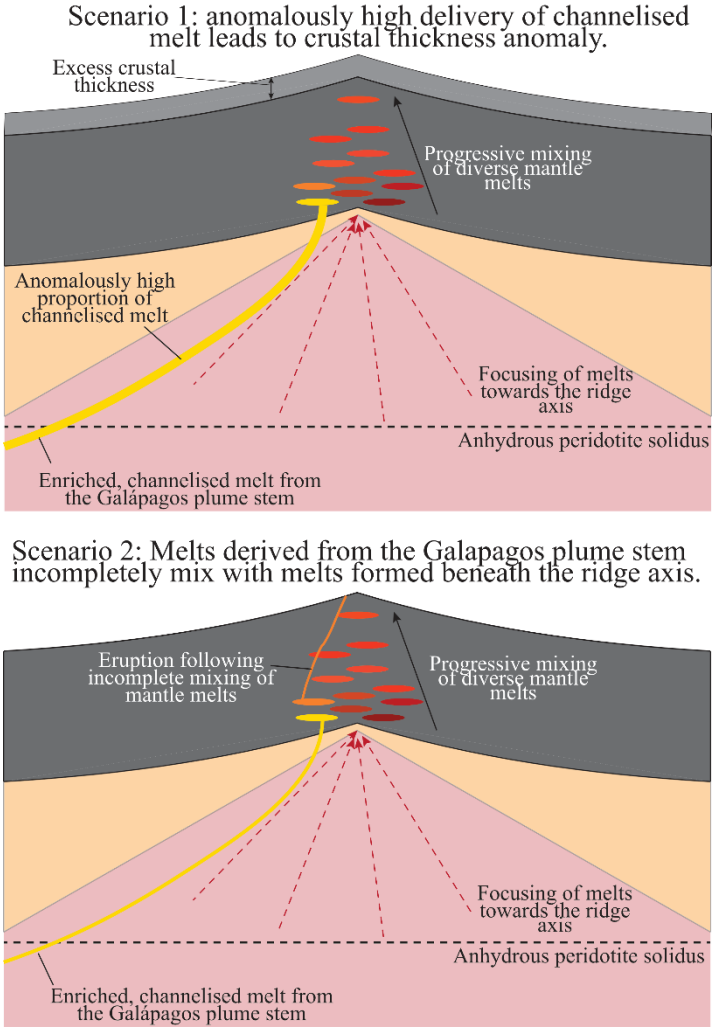

Figure 8 – *Schematic diagram displaying the two ways in which delivery of channelised melt might contribute to the geochemical and geophysical parameters (such as crustal thickness) observed along the GSC. In Scenario 1, an anomalously high flux of channelised melt to the GSC results in moderately-to-highly enriched basalts at the surface and anomalously thick crust (e.g. at the intersection of the WDL with the GSC). In scenario 2, only a moderate supply of channelised melt exists. However, some of this channelised melt manages to ascend and erupt without completely mixing and/or homogenising with melts formed beneath the ridge axis leading to the presence of anomalously enriched basalts at the surface.*

7 QUANTIFYING THE OUTFLUX OF H_2O ON PLUME-INFLUENCED SECTIONS OF THE GALÁPAGOS SPREADING CENTRE

Our new volatile data expand the small number of analyses previously published for the eastern GSC (e.g. Byers et al., 1983), and extend the existing GSC database of volatile element analyses to cover the entire region of plume-influenced ridge. Nevertheless, for much of the plume-influenced section of the GSC, volatile data for basalts remains absent and we thus use the available fractional crystallisation corrected H_2O data from both the eastern and western GSC to identify a non-volatile

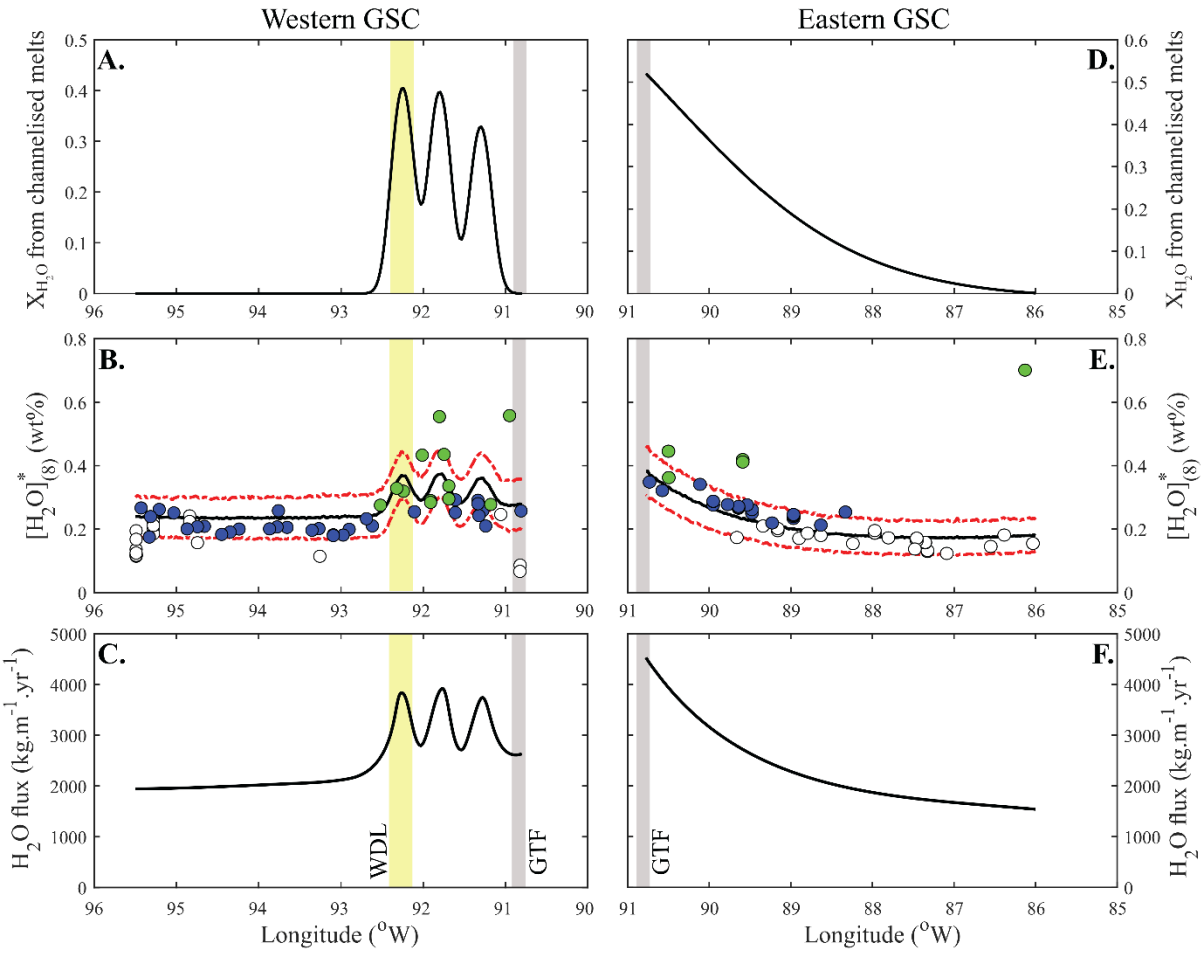

Figure 9 – *H_2O concentrations and fluxes predicted by new models of plume-ridge interaction in the Galápagos (models are identical to those shown in Fig. 5). The model accurately recreates the H_2O contents of basalts from both the eastern GSC and the western GSC. The maximum outflux of H_2O along the western GSC is ~4000 kg.m^{-1}.yr^{-1} where the volcanic lineaments intersect the GSC (compared to the background flux of only ~2000 kg.m^{-1}.yr^{-1}). The greatest outflux of H_2O from the GSC is observed on the eastern GSC near the GTF (~4500 kg.m^{-1}.yr^{-1}) and, in this location, over 50% of the H_2O flux out of the GSC is sourced from plume-derived channelized melts.*

trace element proxy that can be used to estimate the H_2O contents of the remaining GSC basalts. The $[H_2O]_{(8)}$ (that is, the water concentration of each sample once it has been fractional crystallisation corrected to 8 wt% MgO) and $[Sm/Yb]_n$ contents of basalts from both the western and eastern GSC display a very strong, positive correlation (r^2=0.907; Fig 3a). As such, we use the $[Sm/Yb]_n$ ratio of the GSC basalts as a proxy for their fractionation corrected H_2O contents ($[H_2O]_{(8)}$). $[Sm/Yb]_n$ is chosen rather than $[Ce/Yb]_n$, as suggested by Gibson and Richards (2018), because our new data shows a small number of highly-enriched basalts from the western GSC have slightly higher $[H_2O]_{(8)}$ at a given $[Ce/Yb]_n$ than the other GSC basalts (Fig. 3b). As a result, the correlation between $[H_2O]_{(8)}$ and $[Ce/Yb]_n$

653 is subtly different for basalts from the eastern and western GSC (gradients of 0.142 and 0.162,
654 respectively; Fig. 3b).

655 Taking our new volatile data from the eastern GSC, together with published volatile data from the
656 western GSC (Cushman et al., 2004; Ingle et al., 2010), and estimated volatile contents based on the
657 trace element content of additional GSC basalts (Christie et al., 2005), we can use our 2 component
658 models of plume-ridge interaction to calculate the outflux of H_2O from plume-influenced sections of
659 the GSC. This is achieved using our along-ridge mantle melting models that incorporate the influence
660 of channelised melt transport and accurately recreate the trace element composition and crustal
661 thickness of the plume-influenced GSC alongside the following equation:

662 $$H_2O^{flux}(kg/(m.yr)) = (C_{H2O}^{mix}(ppm) \times 10^{-6}) \times SR\ (m/yr) \times CT\ (m) \times 2900(kg/m^3)$$

663 Where C_{H2O}^{mix} is the H_2O concentration of the fully homogenized primary mantle melts and *CT* is the
664 crustal thickness produced at each calculation interval along the GSC (calculation step size of ~0.02°).
665 *SR* represents the spreading rate of the GSC (Schilling et al., 2003), and the density of the melt phase
666 is assumed to be ~2900 kg/m^3.

667 Our results indicate that incorporation of enriched material from the Galápagos mantle plume causes
668 the flux of H_2O to increase by a factor of 3 from 86°W to 90.8°W on the eastern GSC (Fig. 9). On the
669 western GSC, the flux of H_2O is greatest in regions where the prominent volcanic lineaments intersect
670 the GSC, although the maximum flux of H_2O from any part of the western GSC (~4000 kg.m^{-1}.yr^{-1}) is
671 lower than the maximum H_2O flux along the eastern GSC (~4500 kg.m^{-1}.yr^{-1}; Fig. 9). In addition, our
672 calculations show that volatile-rich channelized melts contribute up to ~50% of the H_2O and F outflux,
673 from regions of the plume-influenced GSC that are most strongly influenced by the Galápagos mantle
674 plume (Fig. 9; Fig. S.8). In fact, melt channelisation may account for ~25% of the H_2O outflux from the
675 western GSC between 90.8°W and 92.5°W and ~35% of the H_2O outflux between 86°W and 90.8°W
676 on the eastern GSC.

While transport of volatile-rich melts to the GSC has a clear influence on the H_2O and F concentrations of the erupted basalts, little to no variations are seen in the $^3He/^4He$ ratio of these basalts (Graham et al., 2014). This observation required that melts reaching the GSC have much lower $^3He/^4He$ to those forming deep in the plume beneath the western Galápagos Archipelago. The lack of a primordial $^3He/^4He$ signature in plume-influenced GSC basalts may be because: (i) rapid vertical transport of high-pressure melts with elevated $^3He/^4He$ ratios is restricted to the vicinity of the plume stem (Kurz and Geist, 1999; Villagómez et al. 2014; Peterson et al. 2017); or (ii) the 'deep' plume-stem melts that are being transported laterally to the ridge via channelised flow are derived from blebs of recycled lithosphere (as suggested by Gleeson et al., 2020), with similar $^3He/^4He$ ratios to MORBs (e.g. Day et al., 2015). Overall, this should not be considered as a surprise, but provides further evidence to support the interpretation that the chemical (and volatile) enrichment of the GSC basalts results from the delivery of pyroxenitic melts to the ridge, rather than melts of a primordial mantle component. This is because, recycled lithospheric components are often characterised by $^3He/^4He$ ratios between 8 and 0 R/R_A, although recent work on Icelandic basalts had shown that pyroxenitic signatures can be found in basalts with $^3He/^4He>10$ (Rasmussen et al., 2020). Therefore, contribution of melts from recycled lithospheric components are less likely to be apparent in the $^3He/^4He$ ratio of erupted MORB basalts.

8 CONCLUSIONS

Our study uses new analyses of volatiles (H_2O, F, Cl, and S) in basaltic glass chips from the Galápagos Spreading Centre, as well as two-component mantle melting models, to investigate the nature and dynamics of plume-ridge interaction in the Galápagos. The results of this study can be summarized in 4 key points:

1. Solid-state transfer of plume material between the Galápagos mantle plume and adjacent GSC can account for some of the long length-scale (~100 – 1000 km wide) geochemical and geophysical signatures of plume-ridge interaction. However, solid-state plume-ridge

interaction models cannot easily explain the presence of short length-scale (<10 km) geochemical and geophysical heterogeneities.

2. The long and short length-scale features of plume-ridge interaction in the Galapagos are readily explained by plume-ridge interaction models that include the transport of volatile-rich melts to the GSC in melt-dominated channels. We hypothesise that the nature of melt transport is very different between the eastern and western GSC. This difference, where a large number of small melt channels connect the eastern GSC to the Galápagos mantle plume, but the western GSC is connected via a smaller number of much larger melt channels, might be related to the increased plume-ridge distance of the western GSC compared to the eastern GSC..

3. One key feature of plume-influenced ridge segments is the presence of anomalously enriched basalts (i.e. those that are substantially more enriched with respect to their trace element contents than their neighbouring basalts; Gibson and Richards, 2018). The anomalously enriched basalts located along the GSC have been shown to contain large contributions of melt from a pyroxenitic mantle component with anomalously-high Fe isotope ratios (Gleeson et al., 2020). Our new mantle melting models indicate that the composition of the GSC basalts are controlled by the incomplete mixing of channelised, volatile-rich melts from the Galápagos mantle plume with more depleted melts formed in the sub-ridge mantle. The most enriched basalts from the GSC contain a ~40% contribution from channelized, plume-derived melt.

4. Our results indicate that plume-ridge interaction causes the H_2O flux out of the GSC to vary by a factor of ~3, with the greatest outflux observed on the eastern GSC near the Galápagos Transform Fault (up to ~4500 $kg.m^{-1}.yr^{-1}$) or at the intersections of volcanic lineaments with the western GSC (up to ~4000 $kg.m^{-1}.yr^{-1}$). We suggest that delivery of volatile-rich channelised melts to the ridge axis might account for up to ~50% of the H_2O flux out of these regions.

This manuscript has recently been resubmitted to *Geochemistry, Geophysics, Geosystems* following one round of peer-review.

ACKNOWLEDGEMENTS

M.L.M.G. was supported by a NERC (Natural Environmental Research Council) Research Training Student Grant (NE/L002507/1) and S.A.G. by grant RG57434 for research in Galápagos. The Secondary Ion Mass Spectrometry (SIMS) analysis was carried out during a 1-day pilot project at the Edinburgh Ion Microprobe Facility (EIMF), code IMF622/0517. We are grateful to Iris Buisman and Richard Hinton for assistance with EPMA and SIMS analysis, respectively. We thank Mike Stock for his help with data collection and early discussions about the project. We are also grateful to Mark Richards and Tushar Mittal for sharing their thoughts on plume-ridge interaction and the three anonymous reviewers whose constructive comments all greatly improved the quality of our manuscript.

DATA AND CODE AVAILABILITY

Data collected in this study, and the code used to analyse the data, can be found through the Cardiff University institutional repository (ORCA; http://orca.cf.ac.uk/id/eprint/138532). Code and data are also made available via 10.5281/zenodo.4545901.

REFERENCES

Adam, J., Turner, M., Hauri, E.H., Turner, S., 2016. Crystal/melt partitioning of water and other volatiles during the near-solidus melting of mantle peridotite: Comparisons with non-volatile incompatible elements and implications for the generation of intraplate magmatism. Am. Mineral. 101, 876–888. https://doi.org/10.2138/am-2016-5437

Asimow, P.D., Langmuir, C.H., 2003. The importance of water to oceanic mantle melting regimes. Nature 421, 815–820. https://doi.org/10.1038/nature01429

Behn, M.D., Sinton, J.M., Detrick, R.S., 2004. Effect of the Galápagos hotspot on seafloor volcanism along the Galápagos Spreading Center (90.9–97.6°W). Earth Planet. Sci. Lett. 217, 331–347. https://doi.org/10.1016/S0012-821X(03)00611-3

Bianco, T.A., Ito, G., van Hunen, J., Mahoney, J.J., Ballmer, M.D., 2013. Geochemical variations at ridge-centered hotspots caused by variable melting of a veined mantle plume. Earth Planet. Sci. Lett. 371–372, 191–202. https://doi.org/10.1016/j.epsl.2013.03.050

Blacic, T.M., Ito, G., Canales, J.P., Detrick, R.S., Sinton, J., 2004. Constructing the crust along the Galapagos Spreading Center 91.3°-95.5°W: Correlation of seismic layer 2A with axial magma lens and topographic characteristics. J. Geophys. Res. Solid Earth 109. https://doi.org/10.1029/2004JB003066

Braun, M.G., Sohn, R.A., 2003. Melt migration in plume–ridge systems. Earth Planet. Sci. Lett. 213, 417–430. https://doi.org/10.1016/S0012-821X(03)00279-6

757 Byers, C.D., Muenow, D.W., Garcia, M.O., 1983. Volatiles in basalts and andesites from the Galapagos
758 Spreading Center, 85° to 86°W. Geochim. Cosmochim. Acta 47, 1551–1558.
759 https://doi.org/10.1016/0016-7037(83)90181-3
760 Cabral, R.A., Jackson, M.G., Koga, K.T., Rose-Koga, E.F., Hauri, E.H., Whitehouse, M.J., Price, A.A., Day,
761 J.M.D., Shimizu, N., Kelley, K.A., 2014. Volatile cycling of H_2O, CO_2 , F, and Cl in the HIMU
762 mantle: A new window provided by melt inclusions from oceanic hot spot lavas at Mangaia,
763 Cook Islands. Geochem. Geophys. Geosystems 15, 4445–4467.
764 https://doi.org/10.1002/2014GC005473
765 Canales, J.P., Dunn, R.A., Ito, G., Detrick, R.S., Sallarès, V., 2014. Effect of Variations in Magma Supply
766 on the Crustal Structure of Mid-Ocean Ridges: Insights from the Western Galápagos Spreading
767 Center, in: Harpp, K.S., Mittelstaedt, E., d'Ozouville, N., Graham, D.W. (Eds.), Geophysical
768 Monograph Series. John Wiley & Sons, Inc, Hoboken, New Jersey, pp. 363–391.
769 https://doi.org/10.1002/9781118852538.ch17
770 Canales, J.P., Ito, G., Detrick, R.S., Sinton, J., 2002. Crustal thickness along the western Galápagos
771 Spreading Center and the compensation of the Galápagos hotspot swell. Earth Planet. Sci.
772 Lett. 203, 311–327. https://doi.org/10.1016/S0012-821X(02)00843-9
773 Christie, D.M., Werner, R., Hauff, F., Hoernle, K., Hanan, B.B., 2005. Morphological and geochemical
774 variations along the eastern Galápagos Spreading Center. Geochem. Geophys. Geosystems 6,
775 n/a-n/a. https://doi.org/10.1029/2004GC000714
776 Cushman, B., Sinton, J., Ito, G., Eaby Dixon, J., 2004. Glass compositions, plume-ridge interaction, and
777 hydrous melting along the Galápagos Spreading Center, 90.5°W to 98°W. Geochem. Geophys.
778 Geosystems 5. https://doi.org/10.1029/2004GC000709
779 Dalou, C., Koga, K. T., Shimizu, N., 2012. Experimental determination of F and Cl partitioning between
780 lherzolite and basaltic melt. Contrib. Mineral. Petrol. 163, 591–609.
781 Day, J.M.D., Barry, P.H., Hilton, D.R., Burgess, R., Pearson, D.G., Taylor, L.A., 2015. The helium flux from
782 the continents and ubiquity of low-3He/4He recycled crust and lithosphere. Geochim.
783 Cosmochim. Acta 153, 116–133. https://doi.org/10.1016/j.gca.2015.01.008
784 Detrick, R.S., Sinton, J.M., Ito, G., Canales, J.P., Behn, M., Blacic, T., Cushman, B., Dixon, J.E., Graham,
785 D.W., Mahoney, J.J., 2002. Correlated geophysical, geochemical, and volcanological
786 manifestations of plume-ridge interaction along the Galápagos Spreading Center. Geochem.
787 Geophys. Geosystems 3, 1–14. https://doi.org/10.1029/2002GC000350
788 Dixon, J.E., 1997. Degassing of alkalic basalts. Am. Mineral. 82, 368–378. https://doi.org/10.2138/am-
789 1997-3-415
790 Dixon, J.E., Bindeman, I.N., Kingsley, R.H., Simons, K.K., Le Roux, P.J., Hajewski, T.R., Swart, P.,
791 Langmuir, C.H., Ryan, J.G., Walowski, K.J., Wada, I., Wallace, P.J., 2017. Light Stable Isotopic
792 Compositions of Enriched Mantle Sources: Resolving the Dehydration Paradox. Geochem.
793 Geophys. Geosystems 18, 3801–3839. https://doi.org/10.1002/2016GC006743
794 Donnelly, K.E., Goldstein, S.L., Langmuir, C.H., Spiegelman, M., 2004. Origin of enriched ocean ridge
795 basalts and implications for mantle dynamics. Earth Planet. Sci. Lett. 226, 347–366.
796 https://doi.org/10.1016/j.epsl.2004.07.019
797 Farnetani, D.G., Richards, M.A., 1995. Thermal entrainment and melting in mantle plumes. Earth
798 Planet. Sci. Lett. 136, 251–267. https://doi.org/10.1016/0012-821X(95)00158-9
799 Geist, D., Naumann, T., Larson, P., 1998. Evolution of Galapagos Magmas: Mantle and Crustal
800 Fractionation without Assimilation. J. Petrol. 39, 953–971.
801 https://doi.org/10.1093/petroj/39.5.953
802 Gibson, S.A., Dale, C.W., Geist, D.J., Day, J.A., Brügmann, G., Harpp, K.S., 2016. The influence of melt
803 flux and crustal processing on Re–Os isotope systematics of ocean island basalts: Constraints
804 from Galápagos. Earth Planet. Sci. Lett. 449, 345–359.
805 https://doi.org/10.1016/j.epsl.2016.05.021

806 Gibson, S.A., Geist, D., 2010. Geochemical and geophysical estimates of lithospheric thickness
807 variation beneath Galápagos. Earth Planet. Sci. Lett. 300, 275–286.
808 https://doi.org/10.1016/j.epsl.2010.10.002
809 Gibson, S.A., Geist, D.J., Richards, M.A., 2015. Mantle plume capture, anchoring, and outflow during
810 Galápagos plume-ridge interaction: Mantle plume capture & outflow. Geochem. Geophys.
811 Geosystems 16, 1634–1655. https://doi.org/10.1002/2015GC005723
812 Gibson, S.A., Richards, M.A., 2018. Delivery of deep-sourced, volatile-rich plume material to the global
813 ridge system. Earth Planet. Sci. Lett. 499, 205–218.
814 https://doi.org/10.1016/j.epsl.2018.07.028
815 Gibson, S.A., Rooks, E.E., Day, J.A., Petrone, C.M., Leat, P.T., 2020. The role of sub-continental mantle
816 as both "sink" and "source" in deep Earth volatile cycles. Geochim. Cosmochim. Acta 275,
817 140–162. https://doi.org/10.1016/j.gca.2020.02.018
818 Gleeson, M.L.M., Gibson, S.A., 2019. Crustal controls on apparent mantle pyroxenite signals in ocean-
819 island basalts. Geology. https://doi.org/10.1130/G45759.1
820 Gleeson, M.L.M., Gibson, S.A., Williams, H.M., 2020. Novel insights from Fe-isotopes into the
821 lithological heterogeneity of Ocean Island Basalts and plume-influenced MORBs. Earth Planet.
822 Sci. Lett. 535, 116114. https://doi.org/10.1016/j.epsl.2020.116114
823 Graham, D.W., Hanan, B.B., Lupton, J.E., Hoernle, K., Werner, R., Christie, D.M., Sinton, J.M., 2014.
824 Helium Isotope Variations and Mantle Plume-Spreading Ridge Interactions Along the
825 Galápagos Spreading Center, in: Harpp, K.S., Mittelstaedt, E., d'Ozouville, N., Graham, D.W.
826 (Eds.), Geophysical Monograph Series. John Wiley & Sons, Inc, Hoboken, New Jersey, pp. 393–
827 414. https://doi.org/10.1002/9781118852538.ch18
828 Hanan, B.B., Graham, D.W., 1996. Lead and Helium Isotope Evidence from Oceanic Basalts for a
829 Common Deep Source of Mantle Plumes. Science 272, 991–995.
830 https://doi.org/10.1126/science.272.5264.991
831 Harpp, K.S., Geist, D.J., Koleszar, A.M., Christensen, B., Lyons, J., Sabga, M., Rollins, N., 2014a. The
832 Geology and Geochemistry of Isla Floreana, Galápagos: A Different Type of Late-Stage Ocean
833 Island Volcanism, in: Harpp, K.S., Mittelstaedt, E., d'Ozouville, N., Graham, D.W. (Eds.),
834 Geophysical Monograph Series. John Wiley & Sons, Inc, Hoboken, New Jersey, pp. 71–117.
835 https://doi.org/10.1002/9781118852538.ch6
836 Harpp, K.S., Hall, P.S., Jackson, M.G., 2014b. Galápagos and Easter: A Tale of Two Hotspots, in: Harpp,
837 K.S., Mittelstaedt, E., d'Ozouville, N., Graham, D.W. (Eds.), Geophysical Monograph Series.
838 John Wiley & Sons, Inc, Hoboken, New Jersey, pp. 27–40.
839 https://doi.org/10.1002/9781118852538.ch3
840 Harpp, K.S., Weis, D., 2020. Insights Into the Origins and Compositions of Mantle Plumes: A
841 Comparison of Galápagos and Hawai'i. Geochem. Geophys. Geosystems 21.
842 https://doi.org/10.1029/2019GC008887
843 Harpp, K.S., White, W.M., 2001. Tracing a mantle plume: Isotopic and trace element variations of
844 Galápagos seamounts. Geochem. Geophys. Geosystems 2, n/a-n/a.
845 https://doi.org/10.1029/2000GC000137
846 Harpp, K.S., Wirth, K.R., Teasdale, R., Blair, S., Reed, L., Barr, J., Pistiner, J., Korich, D., 2014c. Plume-
847 Ridge Interaction in the Galápagos: Perspectives from Wolf, Darwin, and Genovesa Islands, in:
848 Harpp, K.S., Mittelstaedt, E., d'Ozouville, N., Graham, D.W. (Eds.), Geophysical Monograph
849 Series. John Wiley & Sons, Inc, Hoboken, New Jersey, pp. 285–334.
850 https://doi.org/10.1002/9781118852538.ch15
851 Hart, S.R., Hauri, E.H., Oschmann, L.A., Whitehead, J.A., 1992. Mantle Plumes and Entrainment:
852 Isotopic Evidence. Science 256, 517–520. https://doi.org/10.1126/science.256.5056.517
853 Hauri, E., Gaetani, G., Green, T., 2006. Partitioning of water during melting of the Earth's upper mantle
854 at H2O-undersaturated conditions. Earth Planet. Sci. Lett. 248, 715–734.
855 https://doi.org/10.1016/j.epsl.2006.06.014

Herzberg, C., Asimow, P.D., 2008. Petrology of some oceanic island basalts: PRIMELT2.XLS software for primary magma calculation. Geochem. Geophys. Geosystems 9, n/a-n/a. https://doi.org/10.1029/2008GC002057

Hirth, G., Kohlstedt, D., 2003. Rheology of the upper mantle and the mantle wedge: A view from the experimentalists, in: Eiler, J. (Ed.), Geophysical Monograph Series. American Geophysical Union, Washington, D. C., pp. 83–105. https://doi.org/10.1029/138GM06

Hirth, G., Kohlstedt, D.L., 1996. Water in the oceanic upper mantle: implications for rheology, melt extraction and the evolution of the lithosphere. Earth Planet. Sci. Lett. 144, 93–108. https://doi.org/10.1016/0012-821X(96)00154-9

Hoernle, K., Werner, R., Morgan, J.P., Garbe-Schönberg, D., Bryce, J., Mrazek, J., 2000. Existence of complex spatial zonation in the Galápagos plume. Geology 28, 435. https://doi.org/10.1130/0091-7613(2000)28<435:EOCSZI>2.0.CO;2

Hooft, E.E.E., Toomey, D.R., Solomon, S.C., 2003. Anomalously thin transition zone beneath the Galápagos hotspot. Earth Planet. Sci. Lett. 216, 55–64. https://doi.org/10.1016/S0012-821X(03)00517-X

Iacovino, K., Matthews, S., Wieser, P., Moore, G., Bégué, F., 2020. VESIcal Part I: An open-source thermodynamic model engine for mixed volatile (H2O-CO2) solubility in silicate melts (preprint). Earth Sciences. https://doi.org/10.31223/X5D606

Ingle, S., Ito, G., Mahoney, J.J., Chazey, W., Sinton, J., Rotella, M., Christie, D.M., 2010. Mechanisms of geochemical and geophysical variations along the western Galápagos Spreading Center. Geochem. Geophys. Geosystems 11, n/a-n/a. https://doi.org/10.1029/2009GC002694

Ito, G., Bianco, T., 2014. Patterns in Galápagos Magmatism Arising from the Upper Mantle Dynamics of Plume-Ridge Interaction, in: Harpp, K.S., Mittelstaedt, E., d'Ozouville, N., Graham, D.W. (Eds.), Geophysical Monograph Series. John Wiley & Sons, Inc, Hoboken, New Jersey, pp. 245–261. https://doi.org/10.1002/9781118852538.ch13

Ito, G., Lin, J., 1995. Oceanic spreading center–hotspot interactions: Constraints from along-isochron bathymetric and gravity anomalies. Geology 23, 657. https://doi.org/10.1130/0091-7613(1995)023<0657:OSCHIC>2.3.CO;2

Ito, G., Lin, J., Gable, C.W., 1997. Interaction of mantle plumes and migrating mid-ocean ridges: Implications for the Galápagos plume-ridge system. J. Geophys. Res. Solid Earth 102, 15403–15417. https://doi.org/10.1029/97JB01049

Ito, G., Lin, J., Graham, D.W., 2003. Observational and theoretical studies of the dynamics of mantle plume–mid-ocean ridge interaction. Rev. Geophys. 41. https://doi.org/10.1029/2002RG000117

Ito, G., Mahoney, J.J., 2005. Flow and melting of a heterogeneous mantle: 1. Method and importance to the geochemistry of ocean island and mid-ocean ridge basalts. Earth Planet. Sci. Lett. 230, 29–46. https://doi.org/10.1016/j.epsl.2004.10.035

Jackson, M.G., Koga, K.T., Price, A., Konter, J.G., Koppers, A.A.P., Finlayson, V.A., Konrad, K., Hauri, E.H., Kylander-Clark, A., Kelley, K.A., Kendrick, M.A., 2015. Deeply dredged submarine HIMU glasses from the Tuvalu Islands, Polynesia: Implications for volatile budgets of recycled oceanic crust. Geochem. Geophys. Geosystems 16, 3210–3234. https://doi.org/10.1002/2015GC005966

Jarosewich, E., Nelen, J.A., Norberg, J.A., 1980. Reference Samples for Electron Microprobe Analysis*. Geostand. Geoanalytical Res. 4, 43–47. https://doi.org/10.1111/j.1751-908X.1980.tb00273.x

Johnson, E.A., 2006. 6. Water in Nominally Anhydrous Crustal Minerals: Speciation, Concentration, and Geologic Significance, in: Keppler, H., Smyth, J.R. (Eds.), Water in Nominally Anhydrous Minerals. De Gruyter, Berlin, Boston, pp. 117–154. https://doi.org/10.1515/9781501509476-010

Katz, R.F., Spiegelman, M., Langmuir, C.H., 2003. A new parameterization of hydrous mantle melting. Geochem. Geophys. Geosystems 4, n/a-n/a. https://doi.org/10.1029/2002GC000433

906 Katz, R.F., Weatherley, S.M., 2012. Consequences of mantle heterogeneity for melt extraction at mid-
907 ocean ridges. Earth Planet. Sci. Lett. 335–336, 226–237.
908 https://doi.org/10.1016/j.epsl.2012.04.042
909 Kendrick, M.A., Hémond, C., Kamenetsky, V.S., Danyushevsky, L., Devey, C.W., Rodemann, T., Jackson,
910 M.G., Perfit, M.R., 2017. Seawater cycled throughout Earth's mantle in partially serpentinized
911 lithosphere. Nat. Geosci. 10, 222–228. https://doi.org/10.1038/ngeo2902
912 Kendrick, M.A., Jackson, M.G., Hauri, E.H., Phillips, D., 2015. The halogen (F, Cl, Br, I) and H2O
913 systematics of Samoan lavas: Assimilated-seawater, EM2 and high-3He/4He components.
914 Earth Planet. Sci. Lett. 410, 197–209. https://doi.org/10.1016/j.epsl.2014.11.026
915 Kokfelt, T., Lundstrom, C., Hoernle, K., Hauff, F., Werner, R., 2005. Plume–ridge interaction studied at
916 the Galápagos spreading center: Evidence from 226Ra–230Th–238U and 231Pa–235U isotopic
917 disequilibria. Earth Planet. Sci. Lett. 234, 165–187. https://doi.org/10.1016/j.epsl.2005.02.031
918 Koleszar, A.M., Saal, A.E., Hauri, E.H., Nagle, A.N., Liang, Y., Kurz, M.D., 2009. The volatile contents of
919 the Galapagos plume; evidence for H2O and F open system behavior in melt inclusions. Earth
920 Planet. Sci. Lett. 287, 442–452. https://doi.org/10.1016/j.epsl.2009.08.029
921 Kurz, M.D., Curtice, J., Fornari, D., Geist, D., Moreira, M., 2009. Primitive neon from the center of the
922 Galápagos hotspot. Earth Planet. Sci. Lett. 286, 23–34.
923 https://doi.org/10.1016/j.epsl.2009.06.008
924 Kurz, M.D., Geist, D., 1999. Dynamics of the Galapagos hotspot from helium isotope geochemistry.
925 Geochim. Cosmochim. Acta 63, 4139–4156. https://doi.org/10.1016/S0016-7037(99)00314-2
926 Lambart, S., Baker, M.B., Stolper, E.M., 2016. The role of pyroxenite in basalt genesis: Melt-PX, a
927 melting parameterization for mantle pyroxenites between 0.9 and 5 GPa: Melt-PX: Pyroxenite
928 Melting Model. J. Geophys. Res. Solid Earth 121, 5708–5735.
929 https://doi.org/10.1002/2015JB012762
930 Langmuir, C.H., Bender, J.F., 1984. The geochemistry of oceanic basalts in the vicinity of transform
931 faults: Observations and implications. Earth Planet. Sci. Lett. 69, 107–127.
932 https://doi.org/10.1016/0012-821X(84)90077-3
933 Le Roux, P., Shirey, S., Hauri, E., Perfit, M., Bender, J., 2006. The effects of variable sources, processes
934 and contaminants on the composition of northern EPR MORB (8–10°N and 12–14°N):
935 Evidence from volatiles (H2O, CO2, S) and halogens (F, Cl). Earth Planet. Sci. Lett. 251, 209–
936 231. https://doi.org/10.1016/j.epsl.2006.09.012
937 Le Voyer, M., Cottrell, E., Kelley, K.A., Brounce, M., Hauri, E.H., 2015. The effect of primary versus
938 secondary processes on the volatile content of MORB glasses: An example from the equatorial
939 Mid-Atlantic Ridge (5°N-3°S): MORB volatile contents along 5{degree sign}N-3{degree sign}S
940 MAR. J. Geophys. Res. Solid Earth 120, 125–144. https://doi.org/10.1002/2014JB011160
941 Le Voyer, M., Hauri, E.H., Cottrell, E., Kelley, K.A., Salters, V.J.M., Langmuir, C.H., Hilton, D.R., Barry,
942 P.H., Füri, E., 2018. Carbon fluxes and primary magma CO_2 contents along the global mid-
943 ocean ridge system. Geochem. Geophys. Geosystems.
944 https://doi.org/10.1029/2018GC007630
945 Maclennan, J., McKenzie, D., Gronvöld, K., 2001. Plume-driven upwelling under central Iceland. Earth
946 Planet. Sci. Lett. 194, 67–82. https://doi.org/10.1016/S0012-821X(01)00553-2
947 Marks, M.A.W., Kendrick, M.A., Eby, G.N., Zack, T., Wenzel, T., 2017. The F, Cl, Br and I Contents of
948 Reference Glasses BHVO-2G, BIR-1G, BCR-2G, GSD-1G, GSE-1G, NIST SRM 610 and NIST SRM
949 612. Geostand. Geoanalytical Res. 41, 107–122. https://doi.org/10.1111/ggr.12128
950 Métrich, N., Zanon, V., Créon, L., Hildenbrand, A., Moreira, M., Marques, F.O., 2014. Is the 'Azores
951 Hotspot' a Wetspot? Insights from the Geochemistry of Fluid and Melt Inclusions in Olivine of
952 Pico Basalts. J. Petrol. 55, 377–393. https://doi.org/10.1093/petrology/egt071
953 Michael, P., 1995. Regionally distinctive sources of depleted MORB: Evidence from trace elements and
954 H2O. Earth Planet. Sci. Lett. 131, 301–320. https://doi.org/10.1016/0012-821X(95)00023-6

955 Michael, P.J., 1988. The concentration, behavior and storage of H2O in the suboceanic upper mantle:
956 Implications for mantle metasomatism. Geochim. Cosmochim. Acta 52, 555–566.
957 https://doi.org/10.1016/0016-7037(88)90110-X
958 Michael, P.J., Cornell, W.C., 1998. Influence of spreading rate and magma supply on crystallization and
959 assimilation beneath mid-ocean ridges: Evidence from chlorine and major element chemistry
960 of mid-ocean ridge basalts. J. Geophys. Res. Solid Earth 103, 18325–18356.
961 https://doi.org/10.1029/98JB00791
962 Mittal, T., Richards, M.A., 2017. Plume-ridge interaction via melt channelization at Galápagos and
963 other near-ridge hotspot provinces. Geochem. Geophys. Geosystems 18, 1711–1738.
964 https://doi.org/10.1002/2016GC006454
965 Mittelstaedt, E., Soule, A.S., Harpp, K.S., Fornari, D., 2014. Variations in Crustal Thickness, Plate
966 Rigidity, and Volcanic Processes Throughout the Northern Galápagos Volcanic Province, in:
967 Harpp, K.S., Mittelstaedt, E., d'Ozouville, N., Graham, D.W. (Eds.), Geophysical Monograph
968 Series. John Wiley & Sons, Inc, Hoboken, New Jersey, pp. 263–284.
969 https://doi.org/10.1002/9781118852538.ch14
970 Morgan, W.J., 1978. Rodriguez, Darwin, Amsterdam, ..., A second type of Hotspot Island. J. Geophys.
971 Res. 83, 5355. https://doi.org/10.1029/JB083iB11p05355
972 Morgan, W.J., 1971. Convection Plumes in the Lower Mantle. Nature 230, 42–43.
973 https://doi.org/10.1038/230042a0
974 Peterson, M.E., Saal, A.E., Kurz, M.D., Hauri, E.H., Blusztajn, J.S., Harpp, K.S., Werner, R., Geist, D.J.,
975 2017. Submarine Basaltic Glasses from the Galapagos Archipelago: Determining the Volatile
976 Budget of the Mantle Plume. J. Petrol. 58, 1419–1450.
977 https://doi.org/10.1093/petrology/egx059
978 Porter, K.A., White, W.M., 2009. Deep mantle subduction flux. Geochem. Geophys. Geosystems 10,
979 n/a-n/a. https://doi.org/10.1029/2009GC002656
980 Rasmussen, M.B., Halldórsson, S.A., Gibson, S.A., Guðfinnsson, G.H., 2020. Olivine chemistry reveals
981 compositional source heterogeneities within a tilted mantle plume beneath Iceland. Earth
982 Planet. Sci. Lett. 531, 116008. https://doi.org/10.1016/j.epsl.2019.116008
983 Reekie, C.D.J., Jenner, F.E., Smythe, D.J., Hauri, E.H., Bullock, E.S., Williams, H.M., 2019. Sulfide
984 resorption during crustal ascent and degassing of oceanic plateau basalts. Nat. Commun. 10.
985 https://doi.org/10.1038/s41467-018-08001-3
986 Ribe, N.M., 1996. The dynamics of plume-ridge interaction: 2. Off-ridge plumes. J. Geophys. Res. Solid
987 Earth 101, 16195–16204. https://doi.org/10.1029/96JB01187
988 Rosenthal, A., Hauri, E.H., Hirschmann, M.M., 2015. Experimental determination of C, F, and H
989 partitioning between mantle minerals and carbonated basalt, CO 2 /Ba and CO 2 /Nb
990 systematics of partial melting, and the CO 2 contents of basaltic source regions. Earth Planet.
991 Sci. Lett. 412, 77–87. https://doi.org/10.1016/j.epsl.2014.11.044
992 Rudge, J.F., Maclennan, J., Stracke, A., 2013. The geochemical consequences of mixing melts from a
993 heterogeneous mantle. Geochim. Cosmochim. Acta 114, 112–143.
994 https://doi.org/10.1016/j.gca.2013.03.042
995 Ryan, W.B.F., Carbotte, S.M., Coplan, J.O., O'Hara, S., Melkonian, A., Arko, R., Weissel, R.A., Ferrini, V.,
996 Goodwillie, A., Nitsche, F., Bonczkowski, J., Zemsky, R., 2009. Global Multi-Resolution
997 Topography synthesis. Geochem. Geophys. Geosystems 10, n/a-n/a.
998 https://doi.org/10.1029/2008GC002332
999 Saal, A.E., Hauri, E.H., Langmuir, C.H., Perfit, M.R., 2002. Vapour undersaturation in primitive mid-
1000 ocean-ridge basalt and the volatile content of Earth's upper mantle. Nature 419, 451–455.
1001 https://doi.org/10.1038/nature01073
1002 Salters, V.J.M., Stracke, A., 2004. Composition of the depleted mantle. Geochem. Geophys.
1003 Geosystems 5, n/a-n/a. https://doi.org/10.1029/2003GC000597
1004 Schilling, J.-G., 1991. Fluxes and excess temperatures of mantle plumes inferred from their interaction
1005 with migrating mid-ocean ridges. Nature 352, 397–403. https://doi.org/10.1038/352397a0

1006 Schilling, J.-G., Fontignie, D., Blichert-Toft, J., Kingsley, R., Tomza, U., 2003. Pb-Hf-Nd-Sr isotope
1007 variations along the Galápagos Spreading Center (101°-83°W): Constraints on the dispersal of
1008 the Galápagos mantle plume. Geochem. Geophys. Geosystems 4.
1009 https://doi.org/10.1029/2002GC000495
1010 Schilling, J.-G., Kingsley, R.H., Devine, J.D., 1982. Galapagos Hot Spot-Spreading Center System: 1.
1011 Spatial petrological and geochemical variations (83°W-101°W). J. Geophys. Res. Solid Earth
1012 87, 5593–5610. https://doi.org/10.1029/JB087iB07p05593
1013 Shimizu, K., Ito, M., Chang, Q., Miyazaki, T., Ueki, K., Toyama, C., Senda, R., Vaglarov, B.S., Ishikawa,
1014 T., Kimura, J.-I., 2019. Identifying volatile mantle trend with the water–fluorine–cerium
1015 systematics of basaltic glass. Chem. Geol. 522, 283–294.
1016 https://doi.org/10.1016/j.chemgeo.2019.06.014
1017 Shimizu, K., Saal, A.E., Myers, C.E., Nagle, A.N., Hauri, E.H., Forsyth, D.W., Kamenetsky, V.S., Niu, Y.,
1018 2016. Two-component mantle melting-mixing model for the generation of mid-ocean ridge
1019 basalts: Implications for the volatile content of the Pacific upper mantle. Geochim.
1020 Cosmochim. Acta 176, 44–80. https://doi.org/10.1016/j.gca.2015.10.033
1021 Shishkina, T.A., Botcharnikov, R.E., Holtz, F., Almeev, R.R., Jazwa, A.M., Jakubiak, A.A., 2014.
1022 Compositional and pressure effects on the solubility of H2O and CO2 in mafic melts. Chem.
1023 Geol. 388, 112–129. https://doi.org/10.1016/j.chemgeo.2014.09.001
1024 Shishkina, T.A., Botcharnikov, R.E., Holtz, F., Almeev, R.R., Portnyagin, M.V., 2010. Solubility of H2O-
1025 and CO2-bearing fluids in tholeiitic basalts at pressures up to 500MPa. Chem. Geol. 277, 115–
1026 125. https://doi.org/10.1016/j.chemgeo.2010.07.014
1027 Shorttle, O., Maclennan, J., Jones, S.M., 2010. Control of the symmetry of plume-ridge interaction by
1028 spreading ridge geometry. Geochem. Geophys. Geosystems 11, n/a-n/a.
1029 https://doi.org/10.1029/2009GC002986
1030 Sinton, J., Detrick, R., Canales, J.P., Ito, G., Behn, M., 2003. Morphology and segmentation of the
1031 western Galápagos Spreading Center, 90.5°-98°W: Plume-ridge interaction at an intermediate
1032 spreading ridge. Geochem. Geophys. Geosystems 4. https://doi.org/10.1029/2003GC000609
1033 Sinton, J.M., Detrick, R.S., 1992. Mid-ocean ridge magma chambers. J. Geophys. Res. 97, 197.
1034 https://doi.org/10.1029/91JB02508
1035 Sleep, N.H., 1990. Hotspots and mantle plumes: Some phenomenology. J. Geophys. Res. 95, 6715.
1036 https://doi.org/10.1029/JB095iB05p06715
1037 Sobolev, A.V., Hofmann, A.W., Kuzmin, D.V., Yaxley, G.M., Arndt, N.T., Chung, S.-L., Danyushevsky,
1038 L.V., Elliott, T., Frey, F.A., Garcia, M.O., Gurenko, A.A., Kamenetsky, V.S., Kerr, A.C.,
1039 Krivolutskaya, N.A., Matvienkov, V.V., Nikogosian, I.K., Rocholl, A., Sigurdsson, I.A.,
1040 Sushchevskaya, N.M., Teklay, M., 2007. The Amount of Recycled Crust in Sources of Mantle-
1041 Derived Melts 316, 7.
1042 Stracke, A., Bizimis, M., Salters, V.J.M., 2003. Recycling oceanic crust: Quantitative constraints:
1043 RECYCLING OCEANIC CRUST. Geochem. Geophys. Geosystems 4.
1044 https://doi.org/10.1029/2001GC000223
1045 Stroncik, N.A., Devey, C.W., 2011. Recycled gabbro signature in hotspot magmas unveiled by plume–
1046 ridge interactions. Nat. Geosci. 4, 393–397. https://doi.org/10.1038/ngeo1121
1047 Stroncik, N.A., Niedermann, S., Haase, K.M., 2008. Plume–ridge interaction revisited: Evidence for melt
1048 mixing from He, Ne and Ar isotope and abundance systematics. Earth Planet. Sci. Lett. 268,
1049 424–432. https://doi.org/10.1016/j.epsl.2008.01.037
1050 Sun, Z., Xiong, X., Wang, J., Liu, X., Li, L., Ruan, M., Zhang, L., Takahashi, E., 2020. Sulfur abundance and
1051 heterogeneity in the MORB mantle estimated by copper partitioning and sulfur solubility
1052 modelling. Earth Planet. Sci. Lett. 538, 116169. https://doi.org/10.1016/j.epsl.2020.116169
1053 Verma, S.P., Schilling, J.-G., 1982. Galapagos Hot Spot-SPreading Center System: 2. ^{87}SR/ ^{86}SR and
1054 large ion lithophile element variations (85°W-101°W). J. Geophys. Res. Solid Earth 87, 10838–
1055 10856. https://doi.org/10.1029/JB087iB13p10838

1056 Vidito, C., Herzberg, C., Gazel, E., Geist, D., Harpp, K., 2013. Lithological structure of the Galápagos
1057 Plume: Lithological Structure Galpagos Plume. Geochem. Geophys. Geosystems 14, 4214–
1058 4240. https://doi.org/10.1002/ggge.20270
1059 Villagómez, D.R., Toomey, D.R., Geist, D.J., Hooft, E.E.E., Solomon, S.C., 2014. Mantle flow and
1060 multistage melting beneath the Galápagos hotspot revealed by seismic imaging. Nat. Geosci.
1061 7, 151–156. https://doi.org/10.1038/ngeo2062
1062 Weatherley, S.M., Katz, R.F., 2012. Melting and channelized magmatic flow in chemically
1063 heterogeneous, upwelling mantle. Geochem. Geophys. Geosystems 13.
1064 https://doi.org/10.1029/2011GC003989
1065 Weatherley, S.M., Katz, R.F., 2010. Plate-driven mantle dynamics and global patterns of mid-ocean
1066 ridge bathymetry. Geochem. Geophys. Geosystems 11, n/a-n/a.
1067 https://doi.org/10.1029/2010GC003192
1068 Weis, D., Garcia, M.O., Rhodes, J.M., Jellinek, M., Scoates, J.S., 2011. Role of the deep mantle in
1069 generating the compositional asymmetry of the Hawaiian mantle plume. Nat. Geosci. 4, 831–
1070 838. https://doi.org/10.1038/ngeo1328
1071 White, W.M., McBirney, A.R., Duncan, R.A., 1993. Petrology and geochemistry of the Galápagos
1072 Islands: Portrait of a pathological mantle plume. J. Geophys. Res. Solid Earth 98, 19533–19563.
1073 https://doi.org/10.1029/93JB02018
1074 Wieser, P.E., Jenner, F., Edmonds, M., Maclennan, J., Kunz, B.E., 2020. Chalcophile elements track the
1075 fate of sulfur at Kīlauea Volcano, Hawai'i. Geochim. Cosmochim. Acta S0016703720303239.
1076 https://doi.org/10.1016/j.gca.2020.05.018
1077 Workman, R.K., Hart, S.R., 2005. Major and trace element composition of the depleted MORB mantle
1078 (DMM). Earth Planet. Sci. Lett. 231, 53–72. https://doi.org/10.1016/j.epsl.2004.12.005
1079 Workman, R.K., Hauri, E., Hart, S.R., Wang, J., Blusztajn, J., 2006. Volatile and trace elements in basaltic
1080 glasses from Samoa: Implications for water distribution in the mantle. Earth Planet. Sci. Lett.
1081 241, 932–951. https://doi.org/10.1016/j.epsl.2005.10.028
1082

This manuscript has recently been resubmitted to *Geochemistry, Geophysics, Geosystems* following one round of peer-review.

TABLES

Table 1 – Parameters used in the solid-state and melt channelisation models of plume-ridge interaction (shown in Figures 4 and 5, respectively).

	Solid State models		Melt channelisation models	
Parameter	Western GSC	Eastern GSC	Western GSC	Eastern GSC
T_p at GTF (°C)	1352	1357	1343	1357
T_p distal from GTF (°C)	1332	1345	1330	1344
$U_{r\text{-}max}$ at transform fault	5	10	1.3	2.2
A[a]	0.6	0.75	0.5	0.6
B[a]	5	10	1.3	2.2
X_{Pyx}	0.03	0.03	0.035	0.03
$P_{termination}$ (GPa)[b]	0.3	0.3	0.3	0.3
H_2O (peridotite)	140	100	140	100
H_2O (pyroxenite)[c]	950	950	950	950
T_p for generation of channelised melts[d]	n/a	n/a	1400	1400

[a]$U_{r\text{-}max}$ beneath any point of the ridge is calculated according to $U_{r-max} = \exp\left(-\left((Long(°W) - 90.8) \times A\right)\right) \times B$ on the western GSC and $U_{r-max} = \exp\left(-\left(\left(90.8 - Long(°W)\right) \times A\right)\right) \times B$ on the eastern GSC.

[b]$P_{termination}$ (GPa) refers to the pressure at the top of the melt column.

[c]The H_2O concentration of the pyroxenitic component is determined using the trace element composition reported in Gleeson et al. (2020). Other, less enriched and thus less hydrous, compositions may also be appropriate, and we thus note that this value does not represent a unique solution.

[d]Channelised melts calculated as the aggregated fractional melt of a pyroxenitic component in the Galápagos plume stem following decompression melting to ~10% (approximately the melt fraction of a pyroxenitic component at the anhydrous peridotite solidus; pyroxenite M5-40; Lambart et al. 2016).